J Adv Ceram

Research Article

Intrinsic properties of dispersion-strengthened HfO_2–Al_2O_3–SiO_2 material as an EBC bond coat

Deteng Wang[1,2], Huiyong Yang[1,2]✉, Qifa Wan[1,2], Yixin Xiao[1,2], Haijiang Yu[1,2], Luyan Wang[1,2], Lianyi Wang[3], Wei Li[2], Ruiying Luo[1,2], Juntong Huang[1,2]✉

Cite this article: Wang D, Yang H, Wan Q, et al. *J Adv Ceram* 2025, **14**(5): 9221066. https://doi.org/10.26599/JAC.2025.9221066

ABSTRACT: To address the challenges of insufficient thermal resistance and high-temperature stability in current environmental barrier coating (EBC) bond coats above 1500 °C, this study successfully synthesized HfO_2–Al_2O_3–SiO_2 powders with a dispersion-strengthened structure for EBC bond coat raw material for spraying through a solid-phase synthesis method using HfO_2, Al_2O_3, and SiO_2 sol. The dispersion-strengthened structure with a microstructure of oxides (HfO_2 and Al_2O_3) dispersed in silicates (mullite and $HfSiO_4$) can be achieved by systematically adjusting the component molar ratios, synthesis temperature, and time. The synthesized raw powders underwent subsequent high-temperature hot-pressing sintering to form ceramic bulks, allowing for a comprehensive characterization of the intrinsic material properties, including thermal conductivity, coefficient of thermal expansion, mechanical performance, oxidation resistance at 1600 °C, and water–oxygen corrosion resistance at 1300 °C. The investigation elucidates the property evolution and related mechanisms, conclusively demonstrating the viability of the HfO_2–Al_2O_3–SiO_2 system as an EBC bond coating material. Additional chemical compatibility tests with SiO_2 at 1500 °C further validated the dispersion-strengthened structure. Notably, oxidation resistance testing at 1600 °C revealed that Al_2O_3 could better capture SiO_2 generated by the decomposition of $HfSiO_4$ to form mullite, thus enhancing the high-temperature stability of the HfO_2–Al_2O_3–SiO_2 material, benefiting from its dispersion-strengthened structure. The present study establishes a robust theoretical foundation for the development of EBC bond coatings with exceptional high-temperature endurance exceeding 1500 °C.

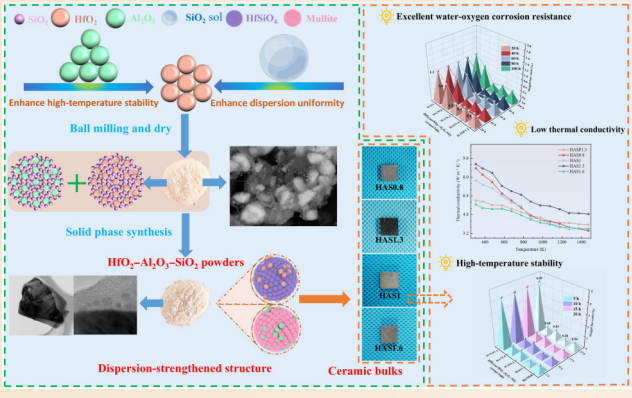

KEYWORDS: HfO_2–Al_2O_3–SiO_2; dispersion-strengthened structure; intrinsic properties; high-temperature properties; oxidation resistance; water–oxygen corrosion

1 Introduction

SiC fiber-reinforced SiC ceramic matrix composites (SiC/SiC CMCs) are considered highly promising materials for engine components owing to their exceptional specific strength, superior mechanical properties, and excellent thermal stability [1–3]. However, in aeroengines, extreme operating conditions, which include high temperatures, corrosive environments, and gas erosion, significantly compromise the surface stability of SiC/SiC CMCs [3–7].

Under dry oxygen conditions, a dense SiO_2 layer formed on the surface of the SiC/SiC CMCs, acting as an effective barrier against further oxidation. This protective layer can prevent oxygen from diffusing into the material, thereby preserving the structural integrity of the composites [2,8]. However, in the presence of water vapor, which is common in engine combustion environments, this SiO_2 layer reacts with water vapor to form volatile $Si(OH)_4$ [9–11], leading to rapid degradation of the SiC/SiC CMCs. The SiC recession process is described by Reactions (1) and (2) [8,9]:

$$2SiC\,(s) + 3O_2 \rightarrow 2SiO_2\,(g) + 2CO\,(g) \quad (1)$$

$$SiO_2 + 2H_2O \rightarrow Si(OH)_4\,(g) \quad (2)$$

To mitigate these challenges, advanced environmental barrier coating (EBC) is essential to protect high-temperature structural material from the adverse effects of engine environments [12–14].

[1] Jiangxi Key Laboratory of Lightweight Composite Materials, Nanchang Hangkong University, Nanchang 330063, China. [2] School of Materials Science and Engineering, Nanchang Hangkong University, Nanchang 330063, China. [3] School of Materials Science and Engineering, Beihang University, Beijing 100191, China.

✉ Corresponding authors. E-mail: H. Yang, yanghuiyong2006@126.com; J. Huang, huangjt@nchu.edu.cn

Received: January 16, 2025; Revised: March 6, 2025; Accepted: March 24, 2025

An EBC system typically consists of a multilayer structure that includes a top coat, an intermediate layer, and a bond coat [13,15–17]. The top coat provides primary protection against corrosive environmental conditions such as water vapor and foreign/domestic damage. The intermediate layer provides temperature gradients to reduce heat and limits the penetration of water vapor and oxygen into the bond coat. The bond coating can prevent the ingress of oxidants such as water vapor and oxygen, reduce the thermal expansion coefficient (CTE) mismatch between adjacent layers, and increase the adhesion strength between layers [15,18]. At present, most research has focused on optimizing the top coat layer, such as disilicate [19,20], monosilicate [17,20], rare earth-modified silicates [21,22], and high-entropy ceramics [23–25]. The development of a bond coat remains a significant challenge in EBC.

Initially, Si was employed as the bond coating material for SiC/SiC composites because of its relatively high melting point of 1416 °C [20,21] and CTE ($(3.5–4.5)\times10^{-6}$ K^{-1}), which closely match those of SiC ($(4.5–5.5)\times10^{-6}$ K^{-1}) [26,27]. However, the CTE mismatch between Si and the SiC/SiC substrate could induce vertical cracks in the coating, which could facilitate the ingress of oxidants at the interface between the EBC bond coat and the top coat. This resulted in the formation of a SiO_2 thermally grown oxide (TGO) layer [16,17,20]. During cooling, the SiO_2 TGO layer transformed from β-cristobalite to an α-phase at approximately 220 °C, causing a 5% volume reduction and leading to channel cracking, especially when the SiO_2 TGO exceeded 1.5 μm in thickness [28]. Additionally, the relatively low melting point of Si increases the risk of coating failure at high temperatures [13,21,28].

To overcome the limitations of traditional Si bond coatings, researchers have developed Si-HfO_2 composite bond coatings by doping Si with HfO_2 [29–34]. This innovation enhanced the resistance of the bond coating to both high temperatures and oxidation. The Si–HfO_2 composite bond coating significantly outperformed pure silicon. Compared with pure silicon, HfO_2 has a melting point of up to 2800 °C [35,36], which greatly enhances the thermal stability of the bond coat. During high-temperature oxidation, HfO_2 reacts with SiO_2 (formed by the oxidation of silicon) to produce $HfSiO_4$. $HfSiO_4$ maintained phase stability up to 1750 °C and exhibited a low oxygen diffusion coefficient, effectively preventing oxygen from penetrating the substrate [37,38]. By adjusting the Si-to-HfO_2 ratio, the CTE of the bond coat could be precisely tailored, thereby minimizing the thermal mismatch stresses between the coating and the substrate [28,33,39].

Despite its advantages, the inclusion of HfO_2 also introduces some challenges [33,39]. It also acts as an efficient oxygen conductor. This characteristic can promote the diffusion of oxygen through the Si-HfO_2 bond coat, potentially leading to the formation of a SiO_2 TGO layer at the interface between the substrate and the coating [29,31,32,34]. Precisely controlling the amount of HfO_2 doped into the Si bond coating presents significant technical difficulties. Variations in the Si/HfO_2 ratio might result in inconsistent performance and stability of EBC [28]. Moreover, the combination of a discontinuous, high-surface-area Si layer and the oxygen-conductive properties of HfO_2 exacerbates the likelihood of TGO formation at the substrate interface, which could compromise the integrity of the entire EBC system by altering its composition and structure. Both the traditional Si bond coating and the Si–HfO_2 composite bond coating exhibit poor resistance to oxidation and SiO_2 TGO corrosion [33,39]. These deficiencies could destabilize the composition and structure of the bond coat, reducing the overall effectiveness of EBC. An excessive HfO_2 content might cause a thermal expansion mismatch, resulting in microcracks within the bond coat. Prolonged heat treatment leads to volume contraction in $HfSiO_4$ [38,40], which induces microporosity. The residual HfO_2 continues to react with the TGO, further destabilizing the bond coat. Furthermore, the efficient oxygen diffusion coefficient of HfO_2 facilitates unwanted oxygen diffusion into the substrate, further weakening the bond coat [33].

Recently, the use of $HfSiO_4$ as a bond coating has been proposed because of its potential advantages [40]. However, the chemical reactions between the sprayed raw material HfO_2 and SiO_2 present challenges in achieving complete solid-phase synthesis of $HfSiO_4$ at a 1 : 1 ratio during heat treatment. An excess amount of HfO_2 can easily cause thermal expansion mismatch and microcracks within the bond coat.

To address the limitations of using $HfSiO_4$ as a bond coating, this study proposes a type of HfO_2–Al_2O_3–SiO_2 EBC bond coating raw material with a dispersion-strengthened structure. This approach is based on the significant advantages of $HfSiO_4$, including its high melting point, excellent phase stability, compatibility with SiC substrates in terms of thermal expansion, and low oxygen diffusion coefficient [35,36]. These characteristics make it an ideal candidate for high-temperature applications, especially as a bond coating in EBC. The presence of HfO_2 is inevitable. Its high oxygen diffusion coefficient poses challenges by forming an interconnected diffusion network and promoting reactions with SiO_2 (from TGO or synthetic material), ultimately leading to high-temperature instability [33,39].

In this study, HfO_2, Al_2O_3, and SiO_2 sol were selected as starting materials to synthesize HfO_2–Al_2O_3–SiO_2 powders for spraying via ball milling, drying, and solid-phase synthesis processes. The reason for choosing SiO_2 sol rather than SiO_2 powders as the raw material for synthesis is that the SiO_2 in the sol is uniformly dispersed at the nanoscale, which allows it to more easily adsorb on the surface of HfO_2 and Al_2O_3 particles. The advantages of this approach are twofold: First, it facilitates the formation of silicates on the surface of Al_2O_3 and HfO_2, and second, it helps prevent the agglomeration of Al_2O_3 and HfO_2 during drying after ball milling and solid-phase synthesis. The preparation process flow chart and the described design tactics for the dispersion-strengthened HfO_2–Al_2O_3–SiO_2 powders are illustrated in Fig. 1. Subsequently, HfO_2–Al_2O_3–SiO_2 ceramic bulks are fabricated through vacuum hot-pressing sintering (VHPS) with the synthesized HfO_2–Al_2O_3–SiO_2 powders. This study examines the impact of the solid-phase synthesis temperature, time, and molar ratio on the reaction products of HfO_2–Al_2O_3–SiO_2 powders, aiming to achieve the desired dispersion-strengthened structure. A systematic investigation is subsequently conducted on the CTE, thermal conductivity, mechanical properties, oxidation resistance at 1600 °C, and water-oxygen corrosion resistance at 1300 °C of the prepared ceramic bulk material, along with their corresponding microstructural mechanisms. These analyses aimed to reveal the feasibility of the HfO_2–Al_2O_3–SiO_2 material system as an EBC bond coating. In future work, on the basis of the findings of this study, the HfO_2–Al_2O_3–SiO_2 powders synthesized in this research will be used to directly coat the surface of SiC/SiC composites through atmospheric plasma spraying. The feasibility and applicability of this system as an EBC bond coating were further validated.

2 Experimental

2.1 Preparation of HfO_2–Al_2O_3–SiO_2 powders and ceramics

Commercially available powders of HfO_2 (1 μm, 99.99 wt%),

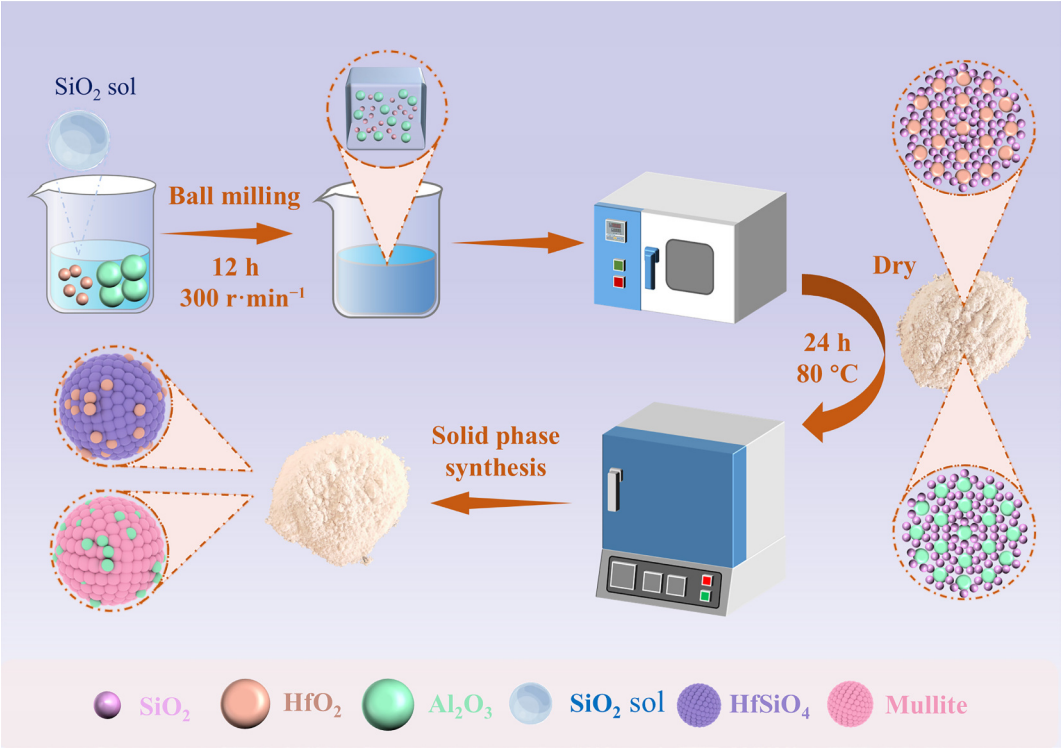

Fig. 1 Preparation process flow chart of dispersion-strengthened HfO_2–Al_2O_3–SiO_2 powders.

Al_2O_3 (1 μm, 99.99 wt%), and SiO_2 sol (15 nm, 25 wt%) (Shanghai Yien Chemical Technology Co., Ltd., China) were used as raw material to synthesize HfO_2–Al_2O_3–SiO_2 powders. In a planetary ball mill, alumina balls and ethanol were used as media for ball milling at 300 r·min^{-1} for 24 h. The obtained slurry was dried at 80 °C for 24 h to obtain uniformly mixed powders. To ensure that SiO_2 is dispersed around HfO_2 and Al_2O_3 with appropriate component contents, different molar ratios were selected to prepare powders. HfO_2–Al_2O_3–SiO_2 powders were prepared via a solid-phase synthesis method. The synthesized HfO_2–Al_2O_3–SiO_2 powders were placed in a graphite mold at 1500 °C and 35 MPa for 2 h to prepare HfO_2–Al_2O_3–SiO_2 ceramic bulks.

To verify the advantages of the HfO_2–Al_2O_3–SiO_2 material system with a dispersion-strengthened structure, the raw powders and ceramic bulks used as control samples were prepared in the same manner as described above, except that the raw material SiO_2 sol was replaced with SiO_2 powders (2 μm, 99.99 wt%) (Shanghai Yien Chemical Technology Co., Ltd., China). The ceramic bulks prepared with different raw materials and compositions are labeled HASP1.3, HAS0.8, HAS1, HAS1.3, and HAS1.6, where "H", "A", and "S" represent HfO_2, Al_2O_3, and SiO_2 sol, respectively, and "SP" denotes SiO_2 powders.

2.2 Phase composition and microstructure of HfO_2–Al_2O_3–SiO_2 material

The microstructure and elemental distribution were analyzed by a scanning electron microscope (SEM; Sigma 30, ZEISS, Germany) with an energy spectrometer (EDS; TECNAI G220, FEI, USA). The microstructure analysis and elemental mapping of the synthesized HfO_2–Al_2O_3–SiO_2 powders were performed via a scanning transmission electron microscope (TEM; Talos F200X, TEI, USA) with an attached high-angle annular dark-field (HAADF) probe and an EDS.

The phase compositions were determined via an X-ray diffractometer (XRD; D8 Advanced, Bruker, Germany) via Cu Kα radiation with a step size of 0.02° at a scanning rate of 2 (°)/min. On the basis of the principle of the adiabatic method, the crystalline phase content of each phase of the ceramics was analyzed semiquantitatively via the reference intensity ratio (RIR) method, as expressed in Eq. (3) [41]:

$$W_x = I_x / \sum_{i=1}^{N} X_i / \mathrm{RIR}_i \tag{3}$$

In the equation, W_x is the mass fraction of a particular phase in the measured sample, I_x is the integrated intensity of the strongest peak of that phase in the measured sample, N is the total number of phases in the measured sample, X_i is the diffraction peak intensity for every individual phase, and RIR is the integrated intensity of the phase in the measured sample (after mixing the pure substance of that phase with Al_2O_3 in a 1 : 1 mass ratio) divided by the integrated intensity of the strongest peak of Al_2O_3.

Table 1 Raw material and compositions of the prepared ceramic bulks

Sample	HfO_2 : Al_2O_3 : SiO_2	Raw material
HASP1.3	1 : 1 : 1.3	SiO_2 powders
HAS0.8	1 : 1 : 0.8	SiO_2 sol
HAS1	1 : 1 : 1	SiO_2 sol
HAS1.3	1 : 1 : 1.3	SiO_2 sol
HAS1.6	1 : 1 : 1.6	SiO_2 sol

2.3 Thermal and mechanical properties of HfO_2–Al_2O_3–SiO_2 ceramics

The thermal diffusion coefficient (D_{th}) of HfO_2–Al_2O_3–SiO_2 ceramic bulk samples was measured via a laser flash analyzer (LFA457, NETZSCH, Germany) in an argon atmosphere from 400 to 1200 °C. HfO_2–Al_2O_3–SiO_2 ceramic bulks with a size of 10 mm × 10 mm × 3 mm were used and coated with graphite layers to prevent heat radiation. The isobaric heat capacity (c_p) is

calculated through the Neumann-Kopp rule in terms of constituent oxides, according to Ref. [42]. Additionally, ρ of the HfO_2–Al_2O_3–SiO_2 ceramic bulk material was measured via the Archimedes drainage method. Thus, the thermal conductivity (κ) of HfO_2–Al_2O_3–SiO_2 ceramic bulk is obtained according to Eq. (4) [43]:

$$\kappa = D_{th} \times c_p \times \rho \quad (4)$$

where c_p and ρ are the heat capacity and the density of the samples, respectively.

CTE of HfO_2–Al_2O_3–SiO_2 ceramic bulk samples from 400 to 1500 °C with a heating rate of 10 °C·min^{-1} in a nitrogen atmosphere was investigated with a thermal expansion instrument (TMA 402F, NETZSCH, Germany). The ceramic bulks were rectangular bars with dimensions of 3 mm × 4 mm × 25 mm.

The reduced modulus and hardness were characterized via nanoindentation (Hysitron TI 980, Bruker, Germany).

2.4 Oxidation behavior of HfO_2–Al_2O_3–SiO_2 ceramics

To evaluate the oxidation behavior, HfO_2–Al_2O_3–SiO_2 ceramic bulks with dimensions of 3 mm × 10 mm × 10 mm were heat treated in air at 1600 °C for 5, 10, 15, and 20 h, respectively. The variation in sample weight before and after each test was measured with a balance (sensitivity: ±0.1 mg). The percentage change in the cumulative weights (ΔMass%) of the samples is calculated via Eq. (5) [44]:

$$\Delta Mass\% = (M_1 - M_0)/M_0 \quad (5)$$

where M_0 and M_1 are the sample masses before and after oxidation, respectively.

The phase compositions, microstructures, and elemental distributions of the HfO_2–Al_2O_3–SiO_2 ceramic bulks before and after oxidation were analyzed via XRD and SEM with the measurement parameters described in Section 2.2.

2.5 Water-oxygen corrosion behavior of HfO_2–Al_2O_3–SiO_2 ceramic bulks

The ceramic bulks with dimensions of 3 mm × 4 mm × 25 mm were placed in a tube furnace (TL1500, Nanjing Boyuntong Instrument Technology Co., Ltd., China), and the water-oxygen corrosion conditions were 50 vol% H_2O (g)/50 vol% O_2 (g), 1.013×10^5 Pa, and 1300 °C. The exposure times in the water-oxygen environment were 20, 40, 60, 80, and 100 h. After treatment in the water-oxygen environment, the samples were removed from the furnace tube at regular intervals to accurately record the weight. The calculation of the percentage change in cumulative weights is shown in Eq. (5).

2.6 Corrosion resistance of synthesized HfO_2–Al_2O_3–SiO_2 powders against SiO_2

To verify that the designed HfO_2–Al_2O_3–SiO_2 material system has a dispersion-strengthened structure, a different kind of HfO_2–Al_2O_3–SiO_2 powders was synthesized with SiO_2 powders (but not SiO_2 sol) and the same HfO_2 and Al_2O_3 powders as the raw material. The process conditions of ball milling, drying, and solid-phase synthesis were exactly the same, as described in Section 2.1. The ratio of raw material used for synthesis was also identical (HfO_2 : Al_2O_3 : SiO_2 = 1 : 1 : 1.3). The two kinds of synthesized HfO_2–Al_2O_3–SiO_2 powders were mixed with SiO_2 powders at a molar ratio of 1 : 2 and ball milled in a planetary ball mill with alumina balls and ethanol as the medium for 12 h. The obtained slurry was dried at 80 °C for 24 h and subsequently heat-treated at 1500 °C for 5 h under an argon atmosphere.

3 Results and discussion

3.1 Composition and microstructure of synthesized HfO_2–Al_2O_3–SiO_2 powders

The SEM images in Fig. 2 show the mixture of HfO_2/Al_2O_3/SiO_2 after ball milling and drying and before solid-phase synthesis at different molar ratios. EDS analysis revealed that the white phase was HfO_2 (yellow marker), the gray phase with a small grain size was SiO_2 (red marker), and the gray phase with a large grain size was Al_2O_3 (blue marker). When the molar ratio of SiO_2 to HfO_2 and Al_2O_3 is less than or equal to (Figs. 2(a) and 2(b)), the SiO_2 content is relatively low, and the Al_2O_3 distribution is uneven. Upon solid-phase synthesis, Al_2O_3 is uniformly embedded in $HfSiO_4$ (Figs. 9(f) and 9(i)). As the SiO_2 ratio increases, the number and distribution of SiO_2 particles change significantly (from sparse to dominant), resulting in a shift in the microstructure of the HfO_2/Al_2O_3/SiO_2 mixture (Figs. 2(c) and 2(d)). This change indicates that adjusting the SiO_2 content can effectively regulate the phase distribution of the HfO_2, Al_2O_3, and SiO_2 mixtures, thereby influencing the microstructure of the synthesized HfO_2–Al_2O_3–SiO_2 material (Figs. 9(f), 9(i), 9(l), and 9(o)) and further their properties.

The molar ratio of HfO_2 : Al_2O_3 : SiO_2 = 1 : 1 : 1.3 for the HfO_2/Al_2O_3/SiO_2 mixture after ball milling and drying (Fig. 2) was used to synthesize HfO_2–Al_2O_3–SiO_2 powders at different heat treatment temperatures and sintering times. This specific molar ratio was chosen for the simultaneous formation of $HfSiO_4$ and mullite while also retaining HfO_2 and Al_2O_3. By adjusting the SiO_2 content, we can facilitate the reaction between HfO_2 and SiO_2 to form $HfSiO_4$, as well as the reaction between Al_2O_3 and SiO_2 to form mullite. Insufficient SiO_2 prevents the formation of the mullite phase, whereas excessive SiO_2 leads to the complete consumption of HfO_2 and Al_2O_3. Therefore, selecting a molar ratio of HfO_2 : Al_2O_3 : SiO_2 = 1 : 1 : 1.3 can ensure that the necessary reactions occur while retaining a certain amount of unreacted HfO_2 and Al_2O_3.

Figure 3(a) presents the XRD patterns of the HfO_2–Al_2O_3–SiO_2 powders synthesized at various temperatures, along with the standard XRD patterns obtained from powder diffraction files (PDFs) for the $HfSiO_4$ (PDF#97-003-1177), mullite (PDF#97-006-6451), HfO_2 (PDF#04-005-4474), Al_2O_3 (PDF#97-009-2631), and SiO_2 (PDF#97-015-5215) components. The XRD patterns only show the characteristic peaks of the raw material at 1300 °C, indicating that the anticipated solid-phase reactions have not occurred. This suggests that the activation energy required for atomic diffusion and structural rearrangement is insufficient, which prevents the atoms from overcoming the interatomic potential barriers, thus inhibiting the dynamic structural reorganization necessary for phase transformation. As a result, the nucleation and growth of new phases are suppressed. At 1400 °C, HfO_2 reacts with SiO_2 to form $HfSiO_4$, as evidenced by the appearance of $HfSiO_4$ peaks and the concurrent weakening of the HfO_2 and SiO_2 peaks. Interestingly, the new mullite phase does not form at 1400 °C because of insufficient activation energy. Upon increasing the temperature to 1450 °C, characteristic peaks of mullite appear in the XRD pattern, indicating the successful formation of the mullite phase. Concurrently, $HfSiO_4$, HfO_2, and Al_2O_3 are present, as indicated by their respective peaks in Fig. 3(a). Notably, the disappearance of the SiO_2 peak further suggests its

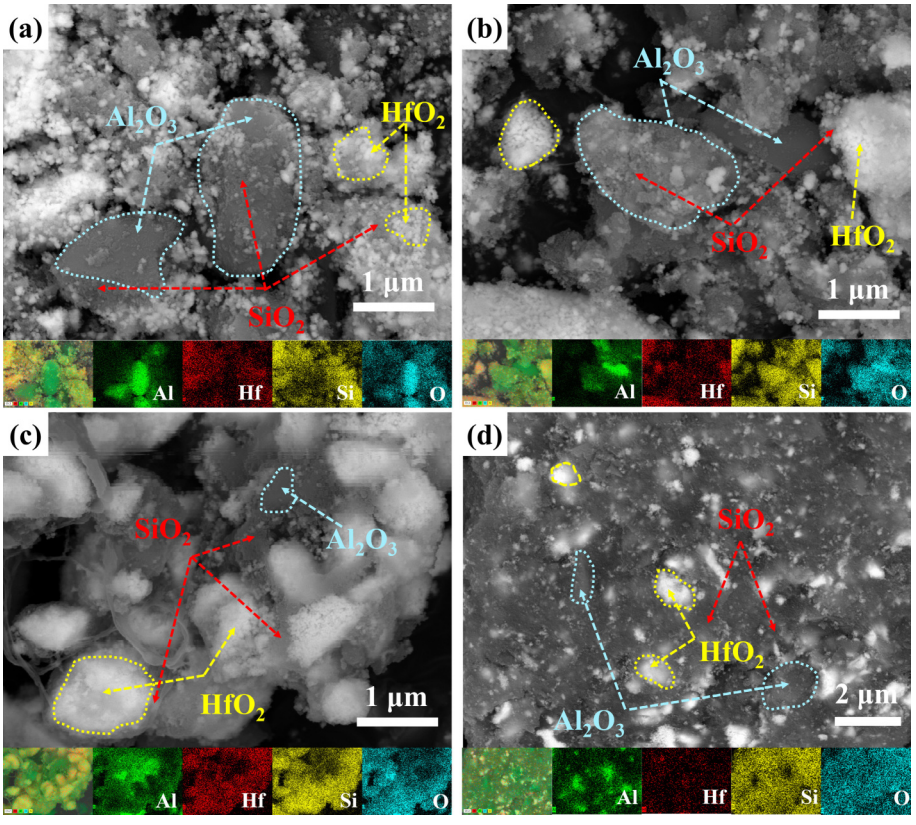

Fig. 2 SEM images of mixture of HfO_2/Al_2O_3/SiO_2 after ball milling and drying and before solid-phase synthesis with different molar ratios: (a) HfO_2 : Al_2O_3 : SiO_2 = 1 : 1 : 0.8, (b) HfO_2 : Al_2O_3 : SiO_2 = 1 : 1 : 1, (c) HfO_2 : Al_2O_3 : SiO_2 = 1 : 1 : 1.3, and (d) HfO_2 : Al_2O_3 : SiO_2 = 1 : 1 : 1.6.

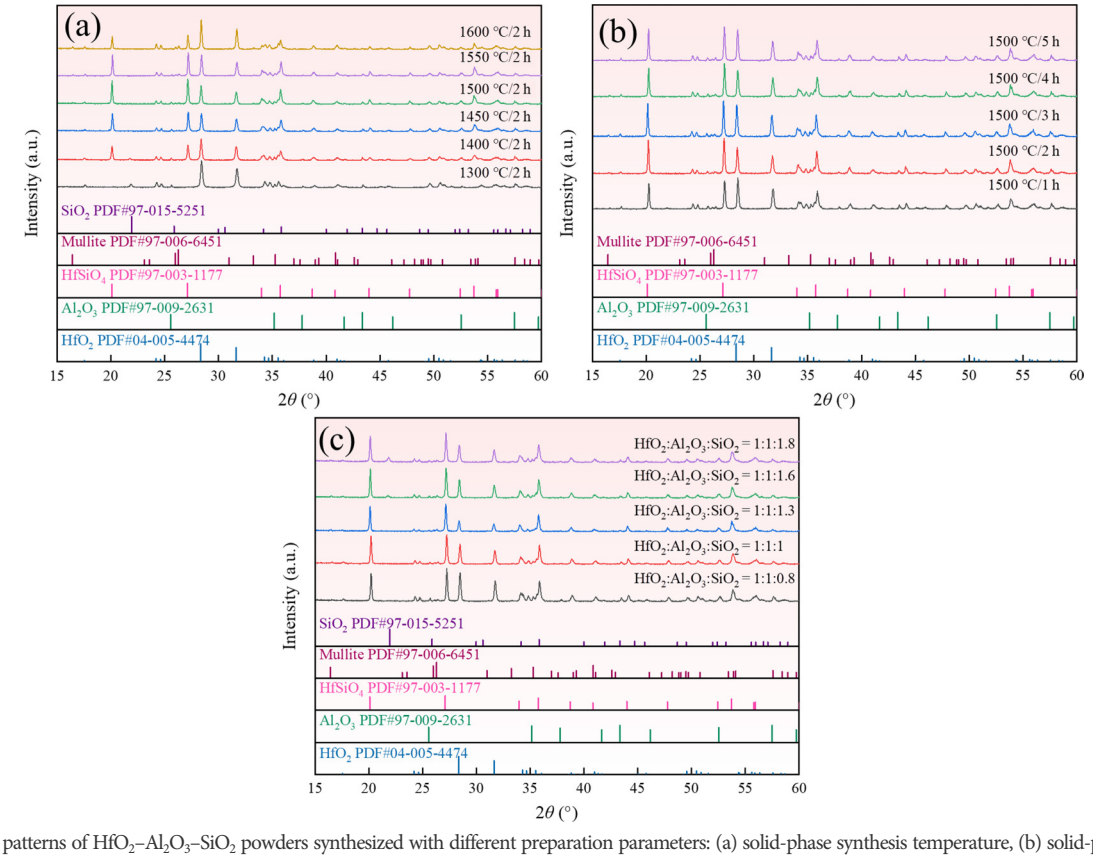

Fig. 3 XRD patterns of HfO_2–Al_2O_3–SiO_2 powders synthesized with different preparation parameters: (a) solid-phase synthesis temperature, (b) solid-phase synthesis time, and (c) molar ratio.

complete consumption, resulting in its transformation into $HfSiO_4$ with HfO_2. As the temperature continues to rise, the characteristic peaks for $HfSiO_4$ and mullite intensify, which signifies that the increased thermal energy allows atoms to overcome kinetic barriers, promoting reconfiguration into a more ordered crystal lattice. This leads to enhanced crystallinity, as evidenced by sharper and stronger diffraction peaks, reflecting better long-range atomic order within the material.

The diffusion rate follows the Arrhenius equation, which describes the exponential relationship between the diffusion coefficient (D) and the absolute temperature (T). Mathematically, this relationship can be expressed mathematically as Eq. (6) [45]:

$$D = D_0 \exp(-Q/(RT)) \tag{6}$$

where D_0 represents the preexponential factor, R is the universal gas constant, and Q is the activation energy.

This equation implies that as the temperature increases, the barrier posed by the activation energy for diffusion progressively diminishes, leading to a rapid increase in the diffusion coefficient. Upon heating to 1600 °C, the intensity of the $HfSiO_4$ diffraction peaks markedly decreases, whereas those of HfO_2 become more prominent. Furthermore, the mullite phase exhibits enhanced crystallinity, likely due to the combined effects of thermal treatment and compositional changes. This phenomenon may be attributed to the diffusion of Al^{3+} exceeding that of Hf^{4+} at 1600 °C and becoming the predominant mechanism.

Figure 3(b) shows the XRD patterns of the HfO_2–Al_2O_3–SiO_2 powders synthesized at each sintering time. At 1500 °C, the system possesses sufficient activation energy to drive the reaction mechanism and facilitate the conversion of reactants to products. As shown in Fig. 3(b), the $HfSiO_4$ and mullite compounds were synthesized via the solid-state reaction method across different sintering durations, with characteristic peaks for HfO_2 and Al_2O_3. As the sintering time increased, the completeness of the chemical reactions increased, and the crystallinity of the $HfSiO_4$ and mullite compounds increased, leading to an increase in their relative abundance. This is evident from the sharper and stronger characteristic peaks for $HfSiO_4$ and mullite. Notably, both mullite and $HfSiO_4$ formed within just 1 h of sintering, indicating a rapid solid-state reaction that reduced energy consumption.

Figure 3(c) presents the XRD patterns of HfO_2–Al_2O_3–SiO_2 powders synthesized at various molar ratios. The characteristic peaks of $HfSiO_4$ and mullite are observed in the HfO_2–Al_2O_3–SiO_2 powders synthesized at various molar ratios. When the molar ratio of SiO_2 to HfO_2 and Al_2O_3 exceeds 1.6, characteristic peaks of residual SiO_2 are observed, indicating incomplete solid phase synthesis. Notably, this residual SiO_2 does not further react with the remaining HfO_2 and Al_2O_3, indirectly confirming the formation of the dispersion strengthened in the HfO_2–Al_2O_3–SiO_2 powders.

A comprehensive analysis revealed that the optimal synthesis conditions were as follows: the molar ratio of HfO_2 : Al_2O_3 : SiO_2 = 1 : 1 : 1.3, the reaction temperature was 1500 °C, and the reaction time was 2 h. The synthesized HfO_2–Al_2O_3–SiO_2 powders contained four components: HfO_2, Al_2O_3, $HfSiO_4$, and mullite, while achieving complete consumption of SiO_2.

To further demonstrate that the synthesized HfO_2–Al_2O_3–SiO_2 powders (at 1500 °C for 2 h with a molar ratio of HfO_2 : Al_2O_3 : SiO_2 = 1 : 1 : 1.3) possess a dispersion-strengthened structure, TEM analysis was performed. As shown in Figs. 4(a) and 4(c), low-magnification bright-field TEM images of the synthesized HfO_2–Al_2O_3–SiO_2 powders reveal various phases. The black regions correspond to $HfSiO_4$, whereas the gray areas indicate the presence of mullite. The light gray regions represent thinner sections of $HfSiO_4$ (Fig. 4(c)). Figure 4(b) shows the EDS elemental mappings of the powders, revealing concentrated distributions of O and Si. In contrast, Hf and Al display well-defined borders, clearly demarcating the boundaries between $HfSiO_4$ and mullite. Figure 4(c) further reveals the particulate structures dispersed within the $HfSiO_4$ matrix. Figure 4(d) presents a high-resolution transmission electron microscopy (HRTEM) image of the selected area in Fig. 4(c), which shows the uniform incorporation of HfO_2 within $HfSiO_4$. Figure 4(e) shows lattice fringes with a spacing of 0.328 nm, corresponding to the (002) plane, and lattice fringes with a spacing of 0.251 nm, corresponding to the $(\bar{2}11)$ plane of $HfSiO_4$. Figure 4(f) presents lattice fringes with a spacing of 0.207 nm, characteristic of the (121) plane, and lattice fringes with a spacing of 0.301 nm, characteristic of the $(\bar{1}12)$ plane of HfO_2. Figure 4(g) displays the selected area electron diffraction (SAED) pattern taken from the marked point "g" in Fig. 4(c), confirming the presence of $HfSiO_4$ in the outer layer. Figure 4(h) shows the presence of Si, Al, O, and Hf (O accounts for 33.69%, Al accounts for 16.31%, Hf accounts for 39.46%, and Si accounts for 10.52%).

Figure 4(i) shows a low-magnification bright-field TEM image of HfO_2–Al_2O_3–SiO_2 powders. In this image, the light gray regions indicate mullite, whereas the dark black areas highlight the presence of Al_2O_3. Al_2O_3 is encapsulated by mullite, with rod-shaped Al_2O_3 grains protruding from this encapsulation, which enhances the mechanical properties and thermal shock resistance of the composite [46]. Figure 4(j) shows the EDS elemental mappings of the powders, revealing concentrated distributions of O and Si. However, Al has distinct boundaries, indicating clear stratification within the powders. Figure 4(k) shows the HRTEM image of the selected area in Fig. 4(i), which reveals that the left portion of the sample is predominantly composed of Al_2O_3, whereas the right portion consists of mullite, with a clear boundary separating the two regions. Figure 4(l) shows lattice fringes with a spacing of 0.255 nm corresponding to the $(\bar{1}11)$ plane and lattice fringes with a spacing of 0.337 nm corresponding to the (210) plane of mullite. Figure 4(m) shows lattice fringes with a spacing of 0.345 nm, characteristic of the (012) plane of Al_2O_3. Figures 4(n) and 4(o) display the SAED images taken from the marked area in Fig. 4(i), which demonstrate that the outer layer is mullite and that the inner layer is Al_2O_3. Figure 4(p) shows the presence of Si, Al, and O (O accounts for 48.13%, Al accounts for 38.99%, and Si accounts for 12.99%). TEM analysis demonstrated that a dispersion-strengthened structure was successfully built in the synthesized HfO_2–Al_2O_3–SiO_2 powders. The absence of detectable Hf characteristic peaks suggests that this region is predominantly composed of Al_2O_3 and mullite.

3.2 Thermal properties of HfO_2–Al_2O_3–SiO_2 ceramic bulks

Thermal properties, including thermal conductivity and CTE, are important parameters that determine the effectiveness of EBC. Figure 5 shows the thermal properties of HfO_2–Al_2O_3–SiO_2 ceramic bulks from 303 to 1473 K. Figure 5(b) shows the c_p curves of HfO_2–Al_2O_3–SiO_2 ceramics according to the Neumann–Kopp rule. c_p (HASP1.3 (2.21–4.41) $J{\cdot}g^{-1}{\cdot}K^{-1}$, HAS0.8 (2.64–4.35) $J{\cdot}g^{-1}{\cdot}K^{-1}$, HAS1 (2.77–4.91) $J{\cdot}g^{-1}{\cdot}K^{-1}$, HAS1.3 (3.77–5.25) $J{\cdot}g^{-1}{\cdot}K^{-1}$, and HAS1.6 (2.43–4.35) $J{\cdot}g^{-1}{\cdot}K^{-1}$) of the HfO_2–Al_2O_3–SiO_2 ceramics increase as the temperature increases from 303 to 1473 K. This increase in the specific heat capacity is attributed to the enhanced phonon scattering caused by the large volume expansion with increasing temperature.

Figure 5(a) shows the thermal diffusivity curves of the prepared

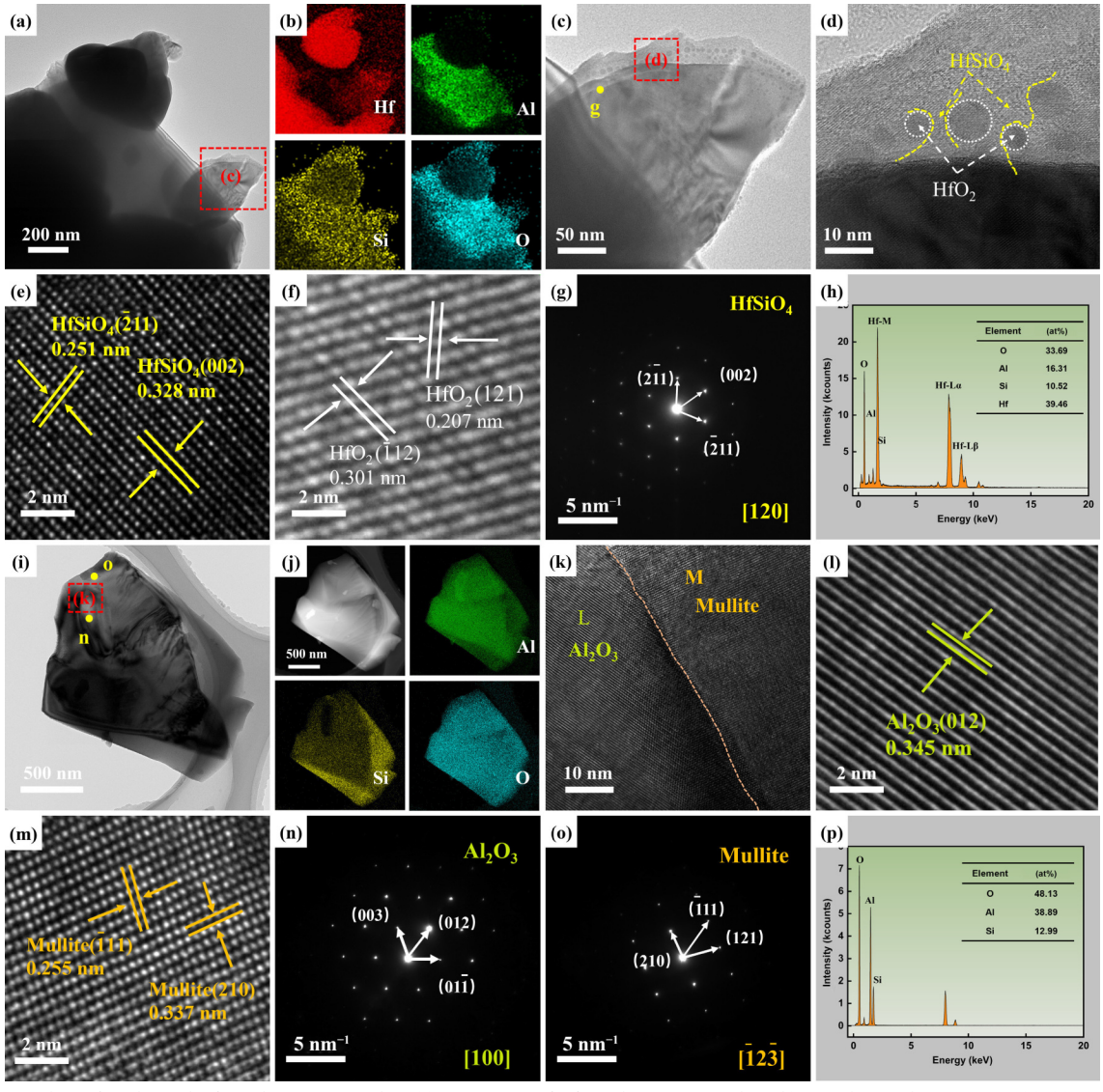

Fig. 4 TEM analysis of synthesized HfO_2–Al_2O_3–SiO_2 powders: (a) TEM image of HfO_2–Al_2O_3–SiO_2 powders, (b) EDS elemental mappings in (a), (c) TEM image of marked in (a), (d) HRTEM image in (c), (e) HRTEM image of $HfSiO_4$, (f) HRTEM image of HfO_2, (g) SAED pattern of $HfSiO_4$, (h) EDS spectrum of (a), (i) TEM image of mullite, (j) EDS elemental mappings in (i), (k) HRTEM image of marked region in (i), (l) HRTEM image of Al_2O_3, (m) HRTEM image of mullite, (n) SAED pattern of Al_2O_3, (o) SAED pattern of mullite, and (p) EDS spectrum in (i).

HfO_2–Al_2O_3–SiO_2 ceramic bulks in the temperature range of 303–1473 K. In contrast to the heat capacity, the thermal diffusivity decreases with increasing temperature. The dispersion-strengthened microstructure of the HfO_2–Al_2O_3–SiO_2 ceramics significantly enhances the inharmonic lattice vibration, strengthens phonon scattering, and effectively reduces the thermal diffusivity. Figure 5(c) displays the thermal conductivity curves of the prepared HfO_2–Al_2O_3–SiO_2 ceramic samples in the temperature range of 303–1473 K. The thermal conductivity of HASP1.3 decreases from 6.01 to 3.95 $W{\cdot}m^{-1}{\cdot}K^{-1}$ as the temperature increases from 303 to 1473 K. The thermal conductivity of HAS0.8 decreases from 8.76 to 3.43 $W{\cdot}m^{-1}{\cdot}K^{-1}$. The thermal conductivity of HAS1 decreases from 7.74 to 3.55 $W{\cdot}m^{-1}{\cdot}K^{-1}$. This value subsequently gradually increases to 3.63 $W{\cdot}m^{-1}{\cdot}K^{-1}$ at 1273 K, which may be attributed to high-temperature thermal radiation. The thermal conductivity of HAS1.3 decreases from 9.12 to 4.85 $W{\cdot}m^{-1}{\cdot}K^{-1}$. The thermal conductivity of HAS1.6 decreases from 5.67 to 3.80 $W{\cdot}m^{-1}{\cdot}K^{-1}$. The thermal conductivities of HASP 1.3, HAS0.8, HAS1, and HAS1.6 are lower than that of HAS1.3. The specific heat capacity and heat diffusion coefficient of each ceramic differ because of the different components and contents of each ceramic.

Figure 8(c) shows the constituent mass fraction of the HfO_2–Al_2O_3–SiO_2 ceramic bulks. It can be observed that the mass fraction of substances varies significantly among ceramics, and the contents of the cations Al^{3+} and Hf^{4+} vary, which also leads to differences in the thermal diffusion and thermal conductivity of the thermal conductivity. In addition, the thermal diffusivity and thermal conductivity of the HfO_2–Al_2O_3–SiO_2 ceramic bulks decrease with increasing temperature, indicating a major contribution from phonon harmonic scattering.

Figure 6 shows the CTE of HfO_2–Al_2O_3–SiO_2 ceramic bulks prepared with different molar ratios between 400 and 1500 °C. Figure 6(a) shows that the CTE of HASP1.3 at 1200 °C is 5.14×10^{-6} $°C^{-1}$ and that at 1400 °C is 4.70×10^{-6} $°C^{-1}$. Figure 6(b) shows that the CTE of HAS0.8 at 1200 °C is 5.15×10^{-6} $°C^{-1}$ and that at 1400 °C is 5.20×10^{-6} $°C^{-1}$. Figure 6(c) shows that the CTE of HAS1 at 1200 °C is 4.55×10^{-6} $°C^{-1}$ and that at 1400 °C is 4.73×10^{-6} $°C^{-1}$. Figure 6(d) shows that the CTE of HAS1.3 at 1200 °C is 4.71×10^{-6} $°C^{-1}$ and that at 1400 °C is 4.83×10^{-6} $°C^{-1}$.

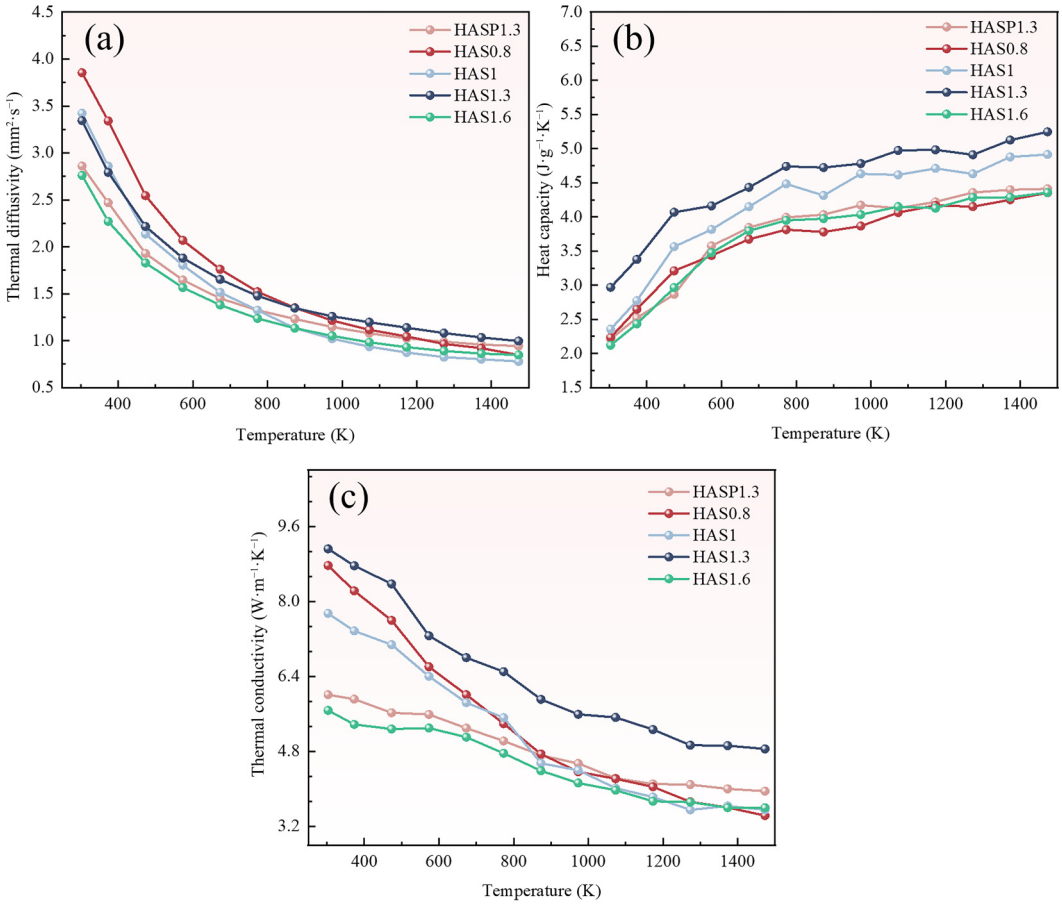

Fig. 5 Thermal properties of HfO_2–Al_2O_3–SiO_2 ceramic bulks: (a) thermal diffusivity, (b) heat capacity, and (c) thermal conductivity.

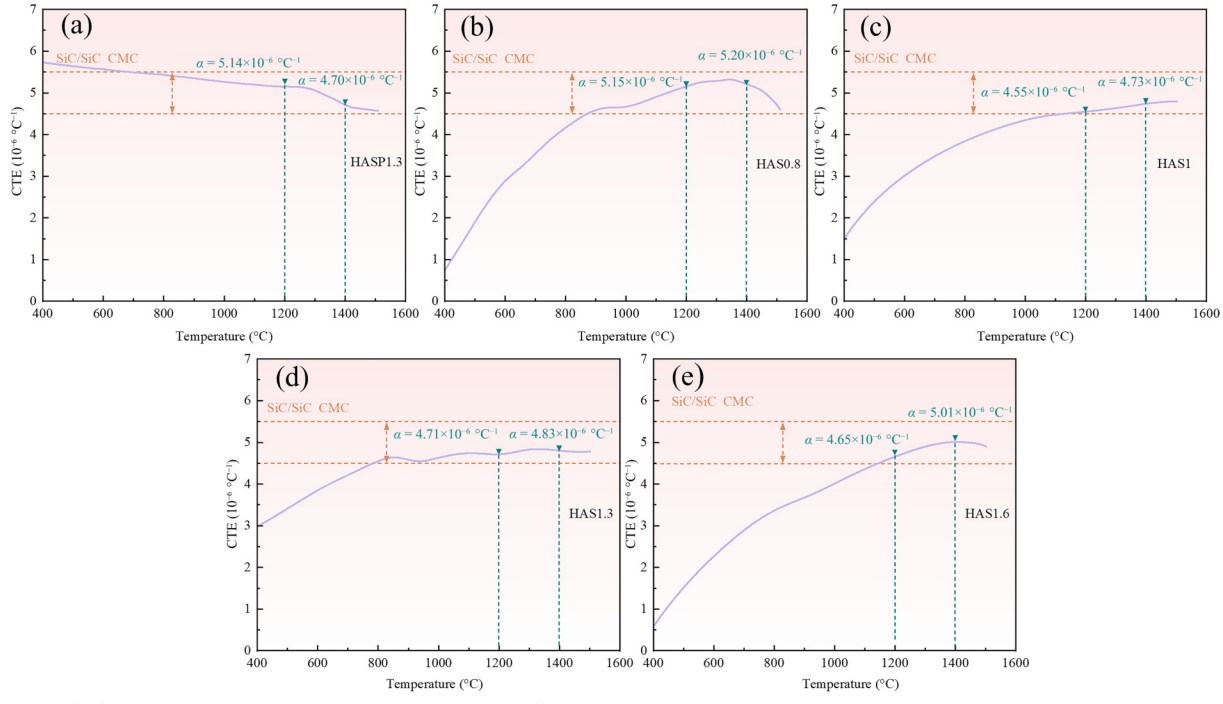

Fig. 6 CTE of HfO_2–Al_2O_3–SiO_2 ceramic bulk material prepared with different molar ratios between 400 and 1500 °C: (a) HASP1.3, (b) HAS0.8, (c) HAS1, (d) HAS1.3, and (e) HAS1.6.

Figure 6(e) indicates that the CTE of HAS1.6 at 1200 °C is 4.65×10^{-6} °C^{-1} and that at 1400 °C is 5.01×10^{-6} °C^{-1}. The coefficients of thermal expansion vary due to the differences in the phase contents of the prepared ceramic bulks (Fig. 8(c)). Hence, the coefficient of thermal expansion can be controlled by adjusting the component content. The prepared HfO_2–Al_2O_3–SiO_2 ceramic bulks are all close to SiC/SiC composites ($(4.5–5.5)\times10^{-6}$ C^{-1}) [26]. Therefore, the HfO_2–Al_2O_3–SiO_2 material system has the most

basic properties as an EBC bond coating. Although the HfO_2–Al_2O_3–SiO_2 material system contains Al_2O_3 and HfO_2, CTEs of $HfSiO_4$ and mullite are both similar to those of SiC/SiC composites, which ensures overall good thermal compatibility between the HfO_2–Al_2O_3–SiO_2 material and SiC/SiC composites.

3.3 Mechanical properties of HfO_2–Al_2O_3–SiO_2 ceramic bulks

In addition to CTE, the elastic reduced moduli and hardness are also critical parameters for EBC. Figure 7(a) shows typical load-displacement curves of HfO_2–Al_2O_3–SiO_2 ceramic bulks measured via nanoindentation tests. A greater slope of the curve indicates greater material hardness. In this case, HASP1.3 has the highest slope, whereas HAS0.8 has the minimum slope. When the load reaches 200 mN, the maximum displacements for each ceramic are as follows: 659 nm (HASP1.3), 973 nm (HAS0.8), 921 nm (HAS1), 882 nm (HAS1.3), and 790 nm (HAS1.6). When the same load is applied to the material, a smaller indenter displacement indicates stronger resistance to localized plastic deformation, indicating greater hardness. This is also reflected in Fig. 7(b). The phase content of the ceramic bulk varied, which resulted in some degree of difference in H and E between the nanoindentation results.

Figure 7(b) shows the reduced moduli and hardness values of the HfO_2–Al_2O_3–SiO_2 ceramic bulks calculated from the nanoindentation curves. The reduced moduli can be approximately equal to the Young's modulus. HASP1.3, prepared with SiO_2 powders, has a greater hardness than the other four samples prepared with SiO_2 sol as the raw material. This is attributed to the formation of mullite with a lower melting point, resulting in fewer pores and higher density than those of the other samples, as discussed in Section 3.4. For HAS0.8-HAS1.6, the hardness increases from 8.11 to 14.17 GPa. This is attributed to the fact that more residual SiO_2 and more produced mullite with a lower melting point jointly enhance the densification and eliminate the pores in the ceramic bulks, as similarly discussed in Section 3.4. The presence of pores reduces the effective load-bearing area and promotes stress concentration, which can lead to localized yielding and crack propagation, thereby reducing the hardness [46]. Consequently, HAS1.6 has a greater hardness and elastic modulus.

3.4 Oxidation behavior of HfO_2–Al_2O_3–SiO_2 ceramic bulks

Figure 8(a) displays the XRD patterns of the HfO_2–Al_2O_3–SiO_2 ceramic bulks prepared with various raw materials and molar ratios (as indicated in Table 1). The XRD analysis of the ceramic samples revealed diffraction peaks for $HfSiO_4$, mullite, HfO_2, and Al_2O_3, confirming their presence in the ceramic bulk. Notably, HAS0.8 and HAS1 lack characteristic peaks for mullite, with Al_2O_3 diffraction peaks being more intense than those in the other ceramic bulks. In contrast, the diffraction peaks of HASP1.3, HAS1.3, and HAS1.6 are indicative of mullite formation, with a reduced intensity of the Al_2O_3 peak. These observations may suggest that during VHPS, Hf^{4+} may diffuse faster than Al^{3+} under a pressure of 35 MPa at 1500 °C, leading to the premature formation of $HfSiO_4$. As a result, the amount of SiO_2 is insufficient to react with Al_2O_3 to form mullite. As the molar ratio increases, the formation of mullite becomes more evident.

Figure 8(b) shows the XRD patterns of the ceramic bulk after oxidation at 1600 °C for 20 h. A comparison with Fig. 8(a) shows that the diffraction peaks corresponding to Al_2O_3 and $HfSiO_4$ decrease, whereas the peaks for HfO_2 and mullite intensify. This observation is further corroborated by Fig. 8(d). The underlying mechanism of this phenomenon is the decomposition of $HfSiO_4$ into HfO_2 and SiO_2, which also leads to the exposure of the Al_2O_3 that is embedded in $HfSiO_4$. At 1600 °C, the diffusion rate of Al^{3+} may exceed that of Hf^{4+}, resulting in Al_2O_3 continuing to react with SiO_2 to form mullite. Consequently, the diffraction peaks of HfO_2 and mullite become significantly more pronounced.

Figures 8(c) and 8(d) show the relative mass fractions of the ceramic bulk before and after oxidation, which was semiquantitatively analyzed via the RIR method in Eq. (3). Upon oxidation at 1600 °C, the relative mass fractions of mullite and HfO_2 increase, whereas those of $HfSiO_4$ and Al_2O_3 decrease (Figs. 8(c) and 8(d)). These compositional changes are also reflected in the XRD patterns.

Figure 8(e) shows the weight loss ratio after different oxidation times. The results indicated that the weight loss ratio of HASP1.3 was significantly greater (4.5 wt%) than those (< 0.8 wt%) of the four ceramic bulk material (HAS0.8, HAS1, HAS1.3, and HAS1.6) prepared with SiO_2 sol as the raw material, among which the weight loss ratio of HAS1 was as low as 0.38 wt%. The mass fractions of mullite and HfO_2 increased, whereas those of $HfSiO_4$ and Al_2O_3 decreased (Figs. 8(c) and 8(d)). This discrepancy arises from microstructural differences. HAS0.8, HAS1, HAS1.3, and HAS1.6, prepared with SiO_2 sol as the raw material, possess a dispersion-strengthened structure with oxides uniformly distributed within the silicates. In contrast, for HASP1.3, prepared with SiO_2 powders as the raw material, the oxides and generated silicates are distributed in a more isolated state. This uniform distribution state of the raw material increases the probability that Al_2O_3 reacts again with SiO_2 produced from the decomposition of $HfSiO_4$ to form mullite. With a high melting point (1910 °C) [47–49], mullite is prone to form a protective layer on the ceramic surface, increasing its resistance to environmental degradation and thereby slowing the weight loss ratio as the oxidation time

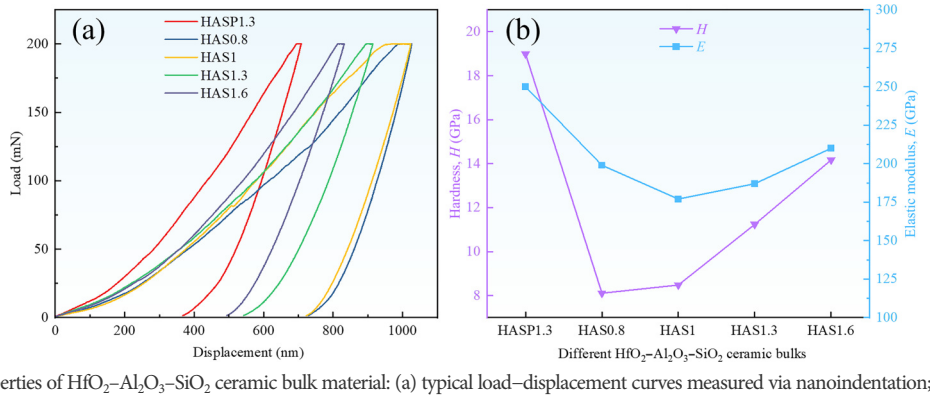

Fig. 7 Mechanical properties of HfO_2–Al_2O_3–SiO_2 ceramic bulk material: (a) typical load–displacement curves measured via nanoindentation; (b) hardness and elastic modulus.

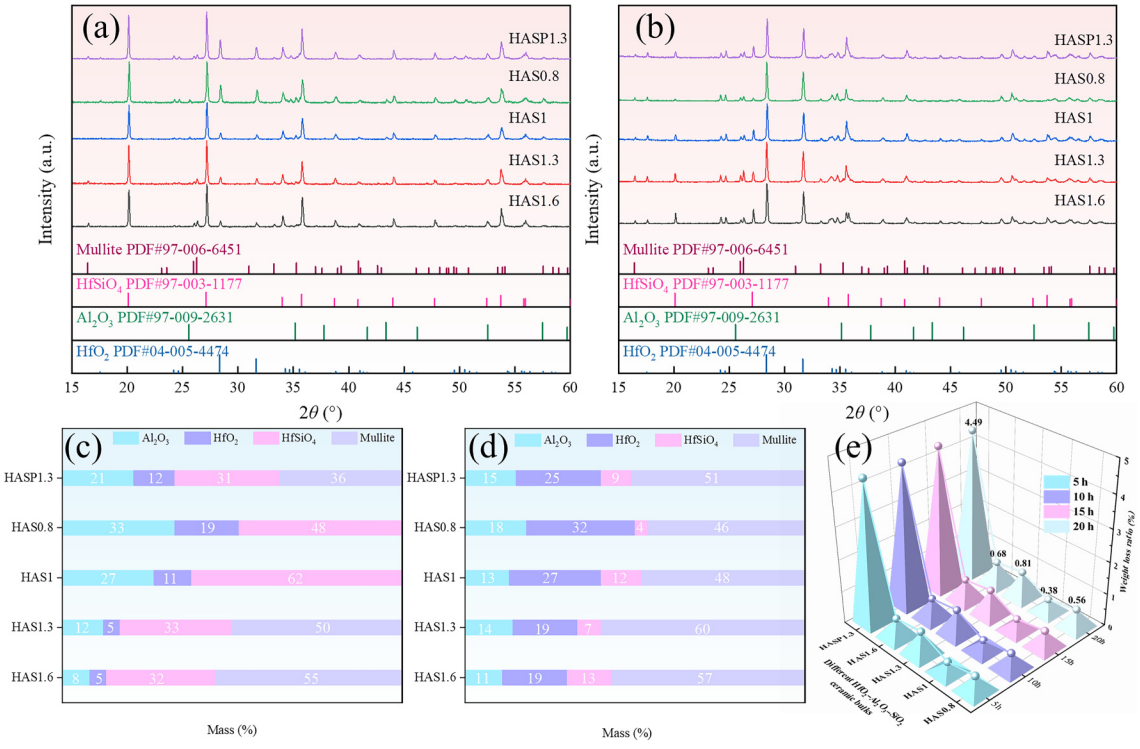

Fig. 8 (a) XRD patterns of HfO_2–Al_2O_3–SiO_2 ceramic bulks prepared from different raw material and molar ratios, (b) XRD patterns of ceramic bulks after oxidation, (c) mass fractions before oxidation, (d) mass fractions after oxidation, and (e) weight loss ratios of HfO_2–Al_2O_3–SiO_2 ceramic bulks.

increases. Hence, the doped Al_2O_3 significantly improves the high-temperature stability through a mechanism that can be summarized as follows: Owing to the phase distribution of oxides dispersed in the silicate, Al_2O_3 is prone to alleviate the high-temperature weight loss by capturing the SiO_2 generated from the decomposition of $HfSiO_4$. Additionally, HAS0.8, HAS1, HAS1.3, and HAS1.6 maintained excellent macroscopic dimensional stability even after oxidation at 1600 °C for 20 h (Figs. 10(d), 10(g), 10(j), and 10(m)), with no significant melting phenomena observed (Figs. 10(f), 10(i), 10(l), and 10(o)). Collectively, these findings demonstrate that this system exhibits good phase stability and an absence of low-melting eutectic formation, which is beneficial for enhancing the high-temperature stability of the EBC bond coating. The results indicate that the incorporation of Al_2O_3 and the microstructure of oxides dispersed in silicates can act synergistically in a 1600 °C oxidation environment, significantly improving the high-temperature oxidation resistance.

Figure 9 shows the macroscopic morphologies, SEM images at different magnifications, and elemental distributions of HASP1.3, HAS0.8, HAS1, HAS1.3, and HAS1.6. Figures 9(e), 9(h), 9(k), and 9(n) specifically display the microstructures and EDS spectra of the HAS0.8, HAS1, HAS1.3, and HAS1.6 samples. The data indicate that the surfaces of the fabricated HfO_2–Al_2O_3–SiO_2 ceramic bulks exhibit pores of varying sizes. Notably, as the molar ratio of SiO_2 to Al_2O_3 and HfO_2 increases, there is a marked reduction in the quantity of pores. On the one hand, this reduction can be attributed to the residual presence of SiO_2 with a relatively lower melting point (~1700 °C) in the synthesized powder raw material (Fig. 3). On the other hand, this reduction can also be attributed to the formation of more mullite, which also has a lower melting point (1800–1900 °C) than Al_2O_3 (~1900 °C) and HfO_2 (~2700 °C). This increase in residual SiO_2 and produced mullite jointly promoted the densification of the ceramic bulk, leading to reduced porosity and improved microstructural integrity. As shown in Fig. 9(b), the microstructure and EDS spectra of HASP1.3 are significantly denser than those of HAS 0.8 and HAS1. The reason for this phenomenon is attributed to the formation of more produced mullite with a lower melting point.

The SEM image of HASP1.3 reveals distinct phase boundaries at higher magnification (Fig. 9(c)). EDS analysis revealed that the white particles were $HfSiO_4$, whereas the black regions corresponded to mullite, with a well-defined interface between the two phases. Figures 9(f) and 9(i) show SEM images of HAS0.8 and HAS1, respectively. EDS analysis indicates that the grayish-white areas correspond to $HfSiO_4$, whereas the black regions are identified as Al_2O_3. These images demonstrate that Al_2O_3 is uniformly embedded within the $HfSiO_4$ matrix, further confirming the successful formation of the dispersion-strengthened structure. Figures 9(l) and 9(o) show SEM images of the HAS1.3 and HAS1.6 ceramics. EDS analysis confirmed that the grayish-white areas were $HfSiO_4$ and that the black regions were mullite.

The HfO_2–Al_2O_3–SiO_2 ceramic bulk samples were subjected to static oxidation treatment at 1600 °C for 20 h in a muffle furnace. The macroscopic morphology and SEM images of the samples prepared from different raw materials and molar ratios after static oxidation treatment are presented in Fig. 10. The SEM images in Fig. 10 show that the HfO_2–Al_2O_3–SiO_2 ceramic bulks are predominantly composed of HfO_2 and mullite, with varying grain sizes and a homogeneous distribution state after oxidation at 1600 °C. The elemental distribution, as observed from surface EDS, reveals an uneven distribution of Si, Hf, Al, and O, with the most pronounced nonuniformity observed in the Al and O. This suggests that Hf predominantly exists in the form of HfO_2, whereas Si is distributed uniformly across the SEM image. This phenomenon is attributed to the decomposition of $HfSiO_4$ during high-temperature oxidation. During this process, $HfSiO_4$ decomposes and releases SiO_2, which then reacts with Al_2O_3 to form a continuous mullite layer on the ceramic surface. This mullite layer effectively isolates HfO_2, thereby reducing the risk of oxygen-related degradation and enhancing the overall stability and performance of the ceramic bulk under oxidative conditions.

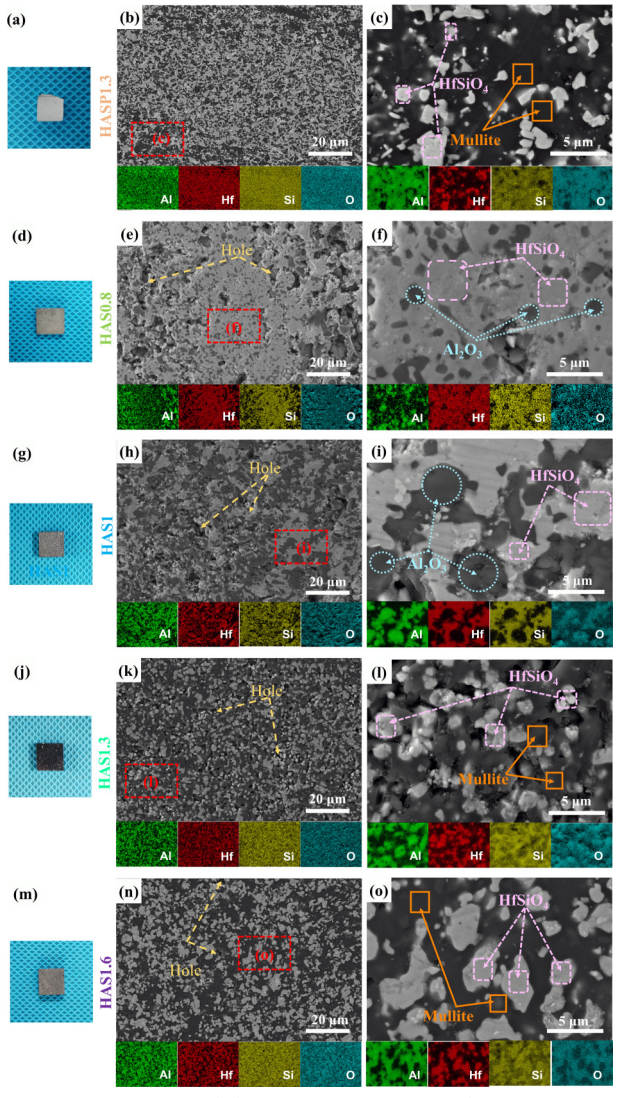

Fig. 9 Macroscopic morphologies, microstructures, and SEM images of HfO_2–Al_2O_3–SiO_2 ceramic bulk material: (a–c) HASP1.3, (d–f) HAS0.8, (g–i) HAS1, (j–l) HAS1.3, and (m–o) HAS1.6.

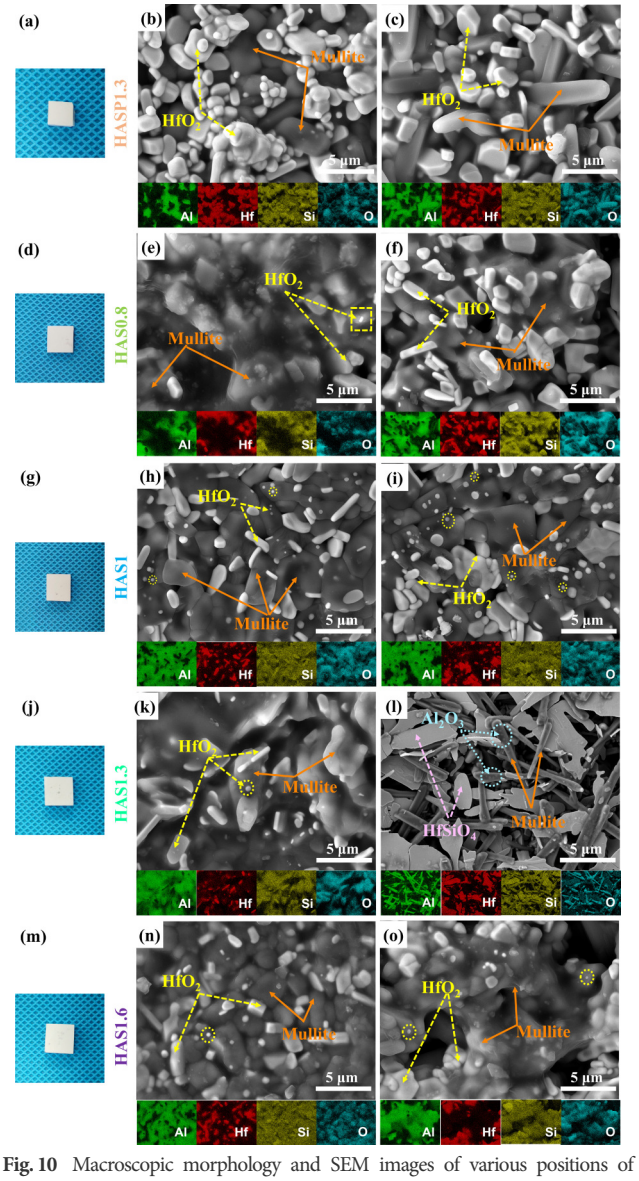

Fig. 10 Macroscopic morphology and SEM images of various positions of ceramic bulk material after oxidation at 1600 °C: (a–c) HASP1.3, (d–f) HAS0.8, (g–i) HAS1, (j–l) HAS1.3, and (m–o) HAS1.6.

In Figs. 10(h), 10(i), 10(k), 10(n), and 10(o), smaller-sized spherical HfO_2 particles are observed. This is attributed to the decomposition of $HfSiO_4$, which has a dispersion-strengthened structure, leading to the release of HfO_2 particles that were originally dispersed within the $HfSiO_4$ matrix. Notably, the HfO_2 grains have not yet fully undergone grain growth, remaining relatively fine and dispersed.

Figure 10(e) indicates that some mullite exists in a gel-like form. The gel-like mullite almost entirely covers the surface, with only a few HfO_2 grains not fully encapsulated. Spherical particles embedded within the rod-like mullite [49] can be observed (Fig. 10(l)). According to the EDS results, these spherical particles are identified as Al_2O_3, which further confirms the existence of a dispersion-strengthened structure in the synthesized HfO_2–Al_2O_3–SiO_2 powders. Additionally, incompletely decomposed $HfSiO_4$ is also present in Fig. 10(l), which is confirmed by the XRD pattern shown in Fig. 8(a).

3.5 Water-oxygen corrosion behavior of HfO_2–Al_2O_3–SiO_2 ceramic bulks

Figure 11(g) shows the XRD patterns of the surface of HfO_2–Al_2O_3–SiO_2 ceramic samples after water-oxygen corrosion. Compared with those in Fig. 7(a), the diffraction peaks of $HfSiO_4$ in HASP1.3 are significantly weakened, the mullite diffraction peaks vanish, and the diffraction peaks of HfO_2 and Al_2O_3 are notably strengthened. However, for the other four samples (HAS0.8, HAS1.0, HAS1.3, and HAS1.6), the $HfSiO_4$ and mullite diffraction peaks are slightly weakened, with corresponding slight increases in the HfO_2 and Al_2O_3 diffraction peaks. Figure 11(h) displays the phase mass fractions after water-oxygen corrosion, which correspond to the changes observed in the XRD patterns (Fig. 11(g)). The $Si(OH)_4$ formed from the decomposition of $HfSiO_4$ and mullite reacts with water vapor [50] (Eqs. (7) and (8) [51,52]), which is easily lost under continuous water vapor flushing. The produced HfO_2 and Al_2O_3 do not react with water vapor and remain on the surface [53].

$$HfSiO_4\,(s) + H_2O\,(g) \rightarrow HfO_2\,(s) + Si(OH)_4\,(g) \quad (7)$$

$$3Al_2O_3 \cdot 2SiO_2 + 6H_2O(g) \rightarrow 3Al_2O_3(s) + 4Si(OH)_4(g) \quad (8)$$

Figure 11(f) displays the phase mass fractions after exposure to water vapor at 1300 °C for 100 h. Due to the lower content of SiO_2

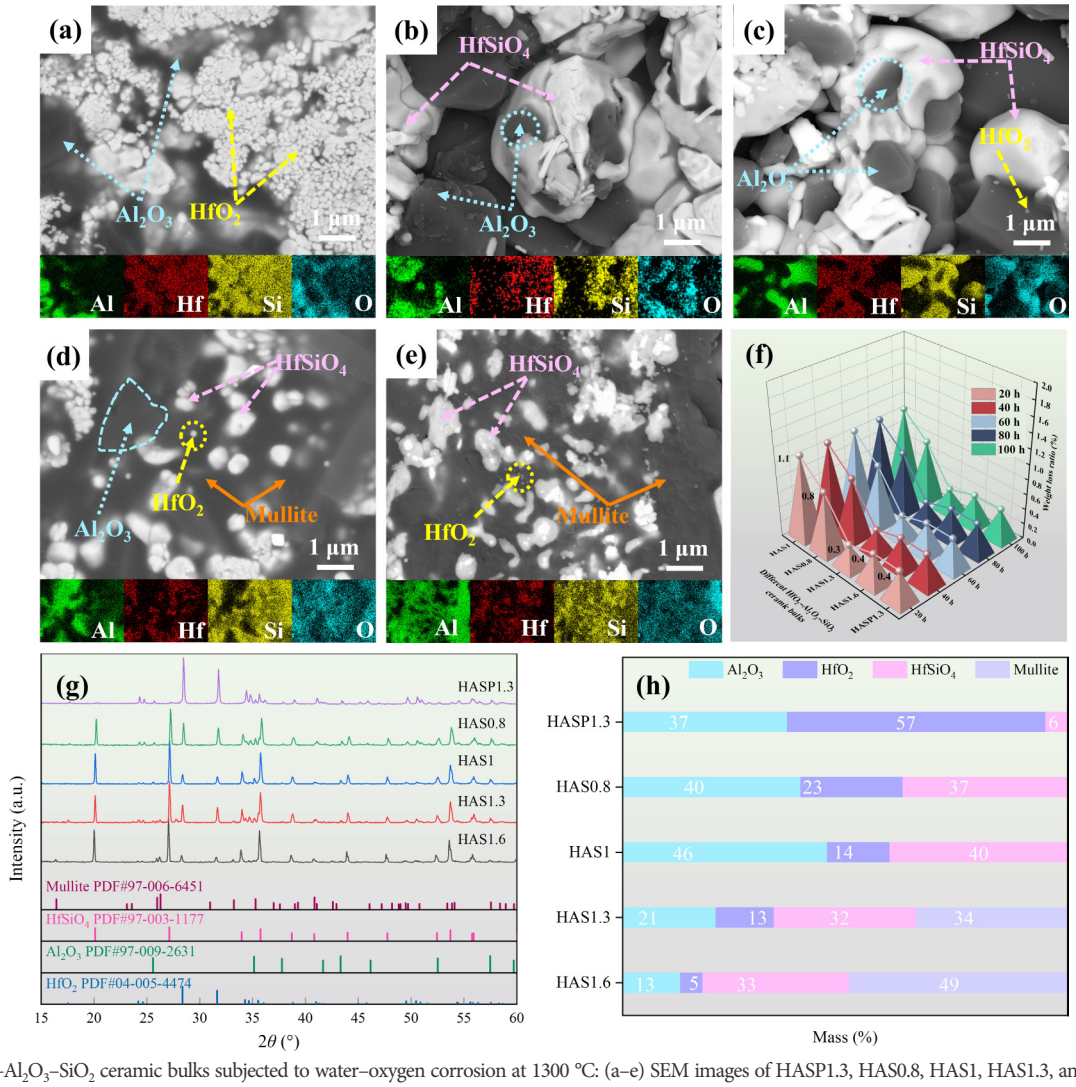

Fig. 11 HfO_2–Al_2O_3–SiO_2 ceramic bulks subjected to water–oxygen corrosion at 1300 °C: (a–e) SEM images of HASP1.3, HAS0.8, HAS1, HAS1.3, and HAS1.6 after water–oxygen corrosion, (f) weight loss ratio after different exposure times, (g) XRD patterns after water-oxygen corrosion for 100 h, and (h) mass fractions after water–oxygen corrosion for 100 h.

sol in the synthesized raw material, fewer low-melting mullite samples are generated, and the residual content of high-melting-point oxides (HfO_2 and Al_2O_3) is relatively high for HAS0.8 and HAS1 (Fig. 8(c)). Additionally, the material exhibits lower densification (Figs. 9(e) and 9(h)), prompting high-temperature water vapor to easily penetrate the internal structure through pores, converting $HfSiO_4$ and mullite into HfO_2 and Al_2O_3. This results in a significantly greater mass loss ratio (Fig. 11(f)). However, for HAS1.3, HAS1.6, and HASP1.3, more low-melting mullite is generated, with fewer high-melting-point oxides remaining (Figs. 8(a)–8(d)). These materials also exhibit a greater degree of densification (Figs. 9(b), 9(k), and 9(n)), making it more difficult for high-temperature water vapor to permeate into the internal structure through pores. Consequently, their weight loss ratios are relatively lower (Fig. 11(f)). These findings indicate that the water-oxygen corrosion resistance of the HfO_2–Al_2O_3–SiO_2 material system can be tailored by adjusting the component content.

Both HASP1.3 and HAS1.3 contain four components ($HfSiO_4$, mullite, HfO_2, and Al_2O_3), as shown in Fig. 8(a). However, their surface compositions and microstructures significantly differ after water-oxygen corrosion, as depicted in Figs. 11(a) and 11(d). For HAS1.3, the surface of the bulk after water-oxygen corrosion retained all four original components (Figs. 11(g) and 11(h)), demonstrating a notably denser microstructure than that of HASP1.3. The dispersion-strengthened structure can be clearly observed, as illustrated in Fig. 11(d). In contrast, after water-oxygen corrosion, HASP1.3 displays a distinctly loose microstructure of HfO_2 and Al_2O_3 on its surface (Fig. 11(a)), with XRD analysis revealing strong oxide diffraction peaks but nearly no silicate peaks (Figs. 11(g) and 11(h)).

The differences in surface composition between HAS1.3 and HASP1.3 after water-oxygen corrosion are due primarily to two factors. First, the HfO_2–Al_2O_3–SiO_2 raw material of HAS1.3 for sintering is SiO_2 sol, which contributes to a more uniform mixing state between SiO_2 and other oxides—HfO_2 and Al_2O_3, resulting in the formation of more low-melting-point mullite and increased densification. This enhanced densification makes it more difficult for high-temperature water vapor to penetrate the material through pores. Consequently, the weight loss caused by water–oxygen corrosion from the reaction of $HfSiO_4$ and mullite at high temperatures is lower for HAS1.3 than for HASP1.3 (Fig. 11(f)), and the surface of HAS1.3 after corrosion contains less HfO_2 and Al_2O_3 (Fig. 11(h)). The second factor lies in the dispersion-strengthened microstructure. Compared with that of HASP1.3, the dispersion-strengthened structure of HAS1.3 reduces the exposure probability of silicates to water–oxygen environments while increasing oxide exposure. Notably, these

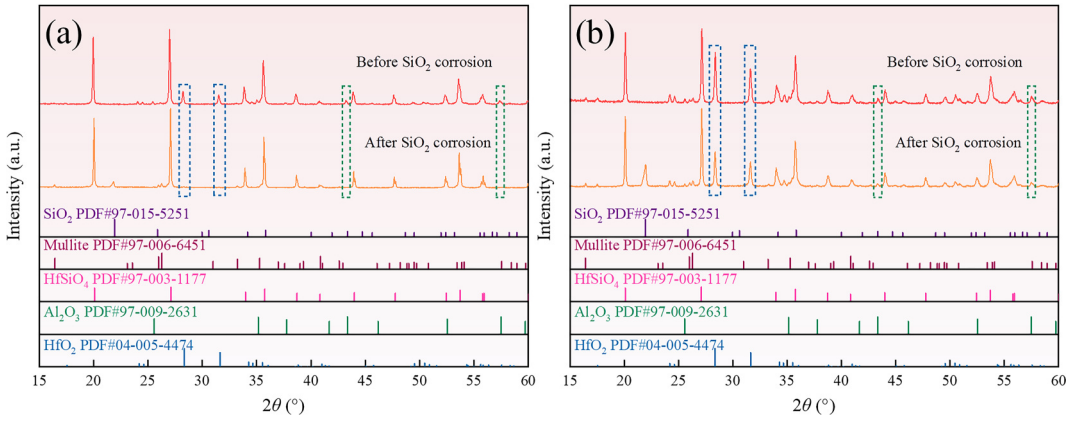

Fig. 12 XRD patterns of synthesized HfO_2–Al_2O_3–SiO_2 powders with different SiO_2 raw materials before and after SiO_2 corrosion: (a) SiO_2 powders and (b) SiO_2 sol.

oxides exhibit exceptional stability against water-oxygen corrosion at 1300 °C.

The distinct surface microstructures of HAS1.3 and HASP1.3 after water-oxygen corrosion originate from the following factors. First, HASP1.3 employs SiO_2 powders as raw material, whereas HAS1.3 utilizes nanoscale SiO_2. This disparity leads to larger silicate phase dimensions in HASP1.3 than in HAS1.3. Second, the dispersion-strengthened microstructure in HAS1.3 significantly reduces the probability of silicate exposure to corrosive environments. Consequently, the combination of coarser silicate grains and higher environmental exposure probability in HASP1.3 promoted the formation of a loose microstructure (Fig. 11(a)). The loose microstructure can accelerate high-temperature water vapor diffusion into the material interior. In contrast, the retention of silicates on the HAS1.3 surface can retain a relatively matched thermal expansion compatibility with SiC/SiC composites, effectively suppressing crack initiation. These results collectively demonstrate that the dispersion-strengthened structure of the designed HfO_2–Al_2O_3–SiO_2 material as a bond coating improves both the water–oxygen corrosion resistance and structural stability at high temperatures.

3.6 Corrosion resistance of synthesized HfO_2–Al_2O_3–SiO_2 powders against SiO_2

Figure 12 shows the XRD patterns of synthesized HfO_2–Al_2O_3–SiO_2 powders prepared from different SiO_2 raw materials before and after SiO_2 corrosion. In Figs. 12(a) and 12(b), diffraction peaks of HfO_2 and Al_2O_3 are observed in the HfO_2–Al_2O_3–SiO_2 powders (using SiO_2 powders as the raw material for synthesis) before corrosion. After SiO_2 corrosion, the HfO_2 and Al_2O_3 diffraction peaks disappeared, whereas the intensities of the $HfSiO_4$ and mullite peaks slightly increased. In contrast, for the HfO_2–Al_2O_3–SiO_2 powders synthesized with SiO_2 sol as the raw material, the diffraction peak intensities of HfO_2 and Al_2O_3 decrease slightly after corrosion, accompanied by a minor increase in the $HfSiO_4$ and mullite peak intensities. A schematic of the mechanism of SiO_2 corrosion on synthesized HfO_2–Al_2O_3–SiO_2 powders with SiO_2 sol as the raw material is shown in Fig. 13.

For the synthesized HfO_2–Al_2O_3–SiO_2 powders with SiO_2 sol as the raw material, the phase distribution state of the oxides dispersed within the silicates significantly reducing the probability of corrosive SiO_2 contacting HfO_2 and Al_2O_3, thereby inhibiting their chemical reactions. Therefore, combined with the TEM analysis (Fig. 4), the SiO_2 corrosion experiment further confirmed the existence of the microstructure of the oxide dispersion-strengthened silicates.

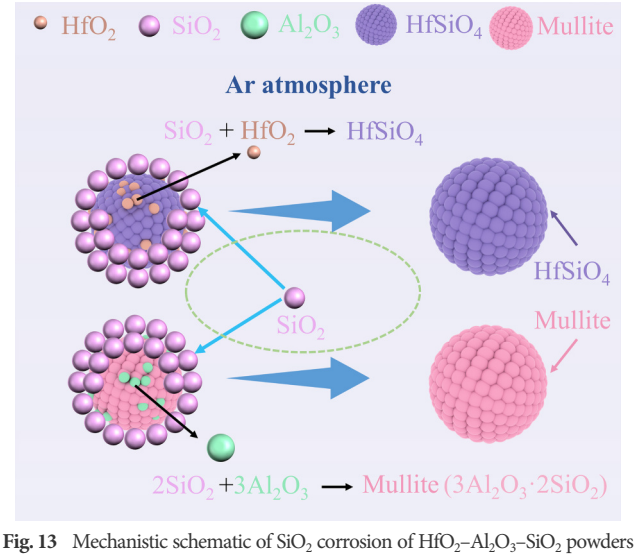

Fig. 13 Mechanistic schematic of SiO_2 corrosion of HfO_2–Al_2O_3–SiO_2 powders synthesized with SiO_2 sol as raw material.

In contrast, for the HfO_2–Al_2O_3–SiO_2 powders synthesized with SiO_2 powders as the raw material, the generated silicates ($HfSiO_4$ and mullite) and residual oxides (HfO_2 and Al_2O_3) are distributed in a relatively isolated state. In high-temperature SiO_2 corrosive environments, the probability of contact between oxides (HfO_2 and Al_2O_3) and the corrosive SiO_2 significantly increases, leading to the formation of more silicates and a reduction in residual oxides (HfO_2 and Al_2O_3). The longer the SiO_2 corrosion time is, the more pronounced this trend becomes. As a result, the peaks of the oxides (HfO_2 and Al_2O_3) nearly disappear, as shown in Fig. 12(a).

This experimental result not only demonstrates that the HfO_2–Al_2O_3–SiO_2 material system has excellent resistance to TGO corrosion but also suggests that the dispersed oxides are more likely to be retained in high-temperature TGO environments and continue to play a role in deflecting or pinning microcracks. Therefore, this excellent SiO_2 corrosion resistance at high temperatures also demonstrates that the designed HfO_2–Al_2O_3–SiO_2 material system possesses excellent high-temperature stability.

4 Conclusions

For the development of EBC bond coats with exceptional high-temperature endurance exceeding 1500 °C, this study synthesized HfO_2–Al_2O_3–SiO_2 powders with a dispersion-strengthened structure for EBC bond coat raw material for spraying through a

solid-phase synthesis method using HfO_2, Al_2O_3, and SiO_2 sol. The synthesized raw powders underwent subsequent high-temperature hot-pressing sintering to form ceramic bulks. The intrinsic material properties, including the thermal conductivity, coefficient of thermal expansion, mechanical performance, oxidation resistance at 1600 °C, and water–oxygen corrosion resistance at 1300 °C, were systematically studied, and the main conclusions are as follows:

(1) By systematically adjusting the molar ratio, solid phase synthesis temperature, and time, the optimal synthesis conditions for synthesizing the designed dispersion-strengthened structure can be identified as follows: the molar ratio of HfO_2 : Al_2O_3 : SiO_2 = 1 : 1 : 1.3, the reaction temperature is 1500 °C, and the reaction time is 2 h. Under the parameters, the synthesized HfO_2–Al_2O_3–SiO_2 powders contained four components: HfO_2, Al_2O_3, $HfSiO_4$, and mullite while achieving complete consumption of SiO_2.

(2) The HfO_2–Al_2O_3–SiO_2 ceramic bulk material exhibits low thermal conductivity (HAS0.8: 3.43–8.76 $W{\cdot}m^{-1}{\cdot}K^{-1}$; HAS1: 3.55–7.74 $W{\cdot}m^{-1}{\cdot}K^{-1}$; HAS1: 4.88–9.12 $W{\cdot}m^{-1}{\cdot}K^{-1}$; HAS1.6: 3.59–5.67 $W{\cdot}m^{-1}{\cdot}K^{-1}$) and demonstrates the excellent thermal expansion compatibility of the HfO_2–Al_2O_3–SiO_2 material system with SiC/SiC CMCs.

(3) Among the four HfO_2–Al_2O_3–SiO_2 ceramic samples (HAS0.8, HAS1.0, HAS1.3, and HAS1.6), the HAS1.6 sample exhibited minimal oxidation mass loss (0.38%) after high-temperature oxidation at 1600 °C for 20 h. The synergistic interaction of i) Al_2O_3 capturing SiO_2 generated by the decomposition of $HfSiO_4$ to form mullite; ii) the microstructure of oxides dispersion-strengthened silicates significantly enhances the high-temperature stability of the HfO_2–Al_2O_3–SiO_2 material system.

(4) Owing to the dispersion-strengthened microstructure, HfO_2–Al_2O_3–SiO_2 ceramic bulks exhibit minimal mass loss (0.3%) after water–vapor corrosion at 1300 °C for 100 h.

(5) HfO_2–Al_2O_3–SiO_2 powders exhibit excellent chemical compatibility with SiO_2 at 1500 °C, further confirming the presence of a dispersion-strengthened microstructure of HfO_2–Al_2O_3–SiO_2 powders.

In conclusion, investigations of the intrinsic properties of the HfO_2–Al_2O_3–SiO_2 material system demonstrate its substantial feasibility as an EBC, positioning it as a promising material system for high-temperature EBC applications requiring operational stability above 1500 °C.

Acknowledgements

The work reported here was funded by the Jiangxi Provincial Natural Science Foundation (20232BAB204019), the National Natural Science Foundation of China (52272063), and the Aeronautical Science Foundation of China (2024Z055056001).

Availability of data and materials

The data that support the findings of this study are available from the corresponding author upon reasonable request.

Competing interests

The authors have no competing interests to declare that are relevant to the content of this article.

References

[1] Naslain RR. SiC-matrix composites: Nonbrittle ceramics for thermo–structural application. *Int J Appl Ceram Tec* 2005, **2**: 75–84.
[2] Padture NP. Advanced structural ceramics in aerospace propulsion. *Nat Mater* 2016, **15**: 804–809.
[3] Song CK, Ye F, Cheng LF, *et al.* Long-term ceramic matrix composite for aeroengine. *J Adv Ceram* 2022, **11**: 1343–1374.
[4] Jacobson NS. Corrosion of silicon-based ceramics in combustion environments. *J Am Ceram Soc* 1993, **76**: 3–28.
[5] Costello JA, Tressler RE. Oxidation kinetics of silicon carbide crystals and ceramics: I, in dry oxygen. *J Am Ceram Soc* 1986, **69**: 674–681.
[6] Naslain R. Challenging ceramic matrix composites for applications in severe environments. *Adv Compos Mater* 1995, **5**: 35–44.
[7] Dos Santos e Lucato SL, Sudre OH, Marshall DB. A method for assessing reactions of water vapor with materials in high-speed, high-temperature flow. *J Am Ceram Soc* 2011, **94**: 186–195.
[8] Smialek JL, Robinson RC, Opila EJ, *et al.* SiC and Si_3N_4 recession due to SiO_2 scale volatility under combustor conditions. *Adv Compos Mater* 1999, **8**: 33–45.
[9] Opila EJ, Hann Jr RE. Paralinear oxidation of CVD SiC in water vapor. *J Am Ceram Soc* 1997, **80**: 197–205.
[10] Xu J, Sarin VK, Dixit S, *et al.* Stability of interfaces in hybrid EBC/TBC coatings for Si-based ceramics in corrosive environments. *Int J Refract Met H* 2015, **49**: 339–349.
[11] Lu YH, Wang YG. Formation and growth of silica layer beneath environmental barrier coatings under water-vapor environment. *J Alloys Compd* 2018, **739**: 817–826.
[12] Cullum G, Schmid T. Ceramic composites for aircraft gas turbine engines. In: Proceedings of the 27th Joint Propulsion Conference, 1991: 1892.
[13] Richards BT, Wadley HNG. Plasma spray deposition of tri-layer environmental barrier coatings. *J Eur Ceram Soc* 2014, **34**: 3069–3083.
[14] Tejero-Martin D, Bennett C, Hussain T. A review on environmental barrier coatings: History, current state of the art and future developments. *J Eur Ceram Soc* 2021, **41**: 1747–1768.
[15] Leisner V, Lange A, Mechnich P, *et al.* Magnetron sputtered Y_2SiO_5 environmental barrier coatings for SiC/SiC CMCS. In: *Advances in High Temperature Ceramic Matrix Compo sites and Materials for Sustainable Development; Ceramic Transactions, Volume CCLXIII.* Singh M, Ohji T, Dong S, Eds. USA: The American Ceramic Society, 2017: 197–209.
[16] Heveran CM, Xu JP, Sarin VK, *et al.* Simulation of stresses in TBC–EBC coating systems for ceramic components in gas turbines. *Surf Coat Tech* 2013, **235**: 354–360.
[17] Padture NP. Environmental degradation of high-temperature protective coatings for ceramic-matrix composites in gas-turbine engines. *npj Mater Degrad* 2019, **3**: 11.
[18] Richards BT, Young KA, de Francqueville F, *et al.* Response of ytterbium disilicate–silicon environmental barrier coatings to thermal cycling in water vapor. *Acta Mater* 2016, **106**: 1–14.
[19] Lee KN, Fox DS, Eldridge JI, *et al.* Upper temperature limit of environmental barrier coatings based on mullite and BSAS. *J Am Ceram Soc* 2003, **86**: 1299–1306.
[20] Abdul-Aziz A. Durability modeling review of thermal- and environmental-barrier-coated fiber-reinforced ceramic matrix composites part I. *Materials* 2018, **11**: 1251.
[21] Lee KN, Miller RA, Jacobson NS. New generation of plasma-sprayed mullite coatings on silicon carbide. *J Am Ceram Soc* 1995, **78**: 705–710.
[22] Lee KN, Fox DS, Bansal NP. Rare earth silicate environmental barrier coatings for SiC/SiC composites and Si_3N_4 ceramics. *J Eur Ceram Soc* 2005, **25**: 1705–1715.
[23] Xiang HM, Xing Y, Dai FZ, *et al.* High-entropy ceramics: Present status, challenges, and a look forward. *J Adv Ceram* 2021, **10**: 385–441.
[24] Zhao ZF, Xiang HM, Chen H, *et al.* High-entropy $(Nd_{0.2}Sm_{0.2}Eu_{0.2}Y_{0.2}Yb_{0.2})_4Al_2O_9$ with good high temperature stability, low thermal conductivity, and anisotropic thermal expansivity. *J Adv Ceram* 2020, **9**: 595–605.
[25] Zhang PX, Duan XJ, Xie XC, *et al.* Xenotime-type high-entropy $(Dy_{1/7}Ho_{1/7}Er_{1/7}Tm_{1/7}Yb_{1/7}Lu_{1/7}Y_{1/7})PO_4$: A promising thermal/

environmental barrier coating material for SiC_f/SiC ceramic matrix composites. *J Adv Ceram* 2023, **12**: 1033–1045.
[26] Olesinski RW, Abbaschian GJ. The C–Si (carbon–silicon) system. *Bull Alloy Phase Diagr* 1984, **5**: 486–489.
[27] Anton R, Leisner V, Watermeyer P, *et al.* Hafnia-doped silicon bond coats manufactured by PVD for SiC/SiC CMCs. *Acta Mater* 2020, **183**: 471–483.
[28] Xiao SK, Li JZ, Liu XR, *et al.* Exploration of the oxidation behavior and doping ratio of the Si–HfO_2 bond layer used in environmental barrier coatings. *Int J Appl Ceram Tec* 2023, **20**: 1753–1763.
[29] Harder BJ. Oxidation performance of Si–HfO_2 environmental barrier coating bond Coats deposited via plasma spray-physical vapor deposition. *Surf Coat Tech* 2020, **384**: 125311.
[30] Deijkers JA, Wadley HNG. Hafnium silicate formation during oxidation of a permeable silicon +HfO_2 powder composite system. *Acta Mater* 2020, **201**: 448–461.
[31] Ding QJ, Tan X, Jiang LW, *et al.* High-temperature performances of Si–HfO_2-based environmental barrier coatings via atmospheric plasma spraying. *Ceram Int* 2022, **48**: 23127–23136.
[32] Yu S, Wang YM, Wang SQ, *et al.* Oxidation behavior and cracking evolution of atmospheric plasma spraying Si and 60Si–40HfO_2 bond coats at 1400 °C. *Ceram Int* 2023, **49**: 33659–33670.
[33] Luo JC, Yang WQ, Chen L, *et al.* Silicon-based bond coatings for environmental barrier coatings: Present status and prospective. *Int J Appl Ceram Tec* 2024, **21**: 3771–3788.
[34] Wang YD, He J, Guo Q, *et al.* Effect of HfO_2 addition on the high-temperature oxidation behavior of Si–HfO_2-based composites at 1300 °C and 1400 °C. *J Alloys Compd* 2025, **1010**: 178261.
[35] Haggerty RP, Sarin P, Apostolov ZD, *et al.* Thermal expansion of HfO_2 and ZrO_2. *J Am Ceram Soc* 2014, **97**: 2213–2222.
[36] Banerjee W, Kashir A, Kamba S. Hafnium oxide (HfO_2)–A multifunctional oxide: A review on the prospect and challenges of hafnium oxide in resistive switching and ferroelectric memories. *Small* 2022, **18**: 2107575.
[37] Deijkers JA, Wadley HNG. Hafnium silicate formation during the reaction of β-cristobalite SiO_2 and monoclinic HfO_2 particles. *J Am Ceram Soc* 2020, **103**: 5400–5410.
[38] Niu JJ, Lu ZY, Nan S, *et al.* Phase transition of hafnon, $HfSiO_4$, at high pressure. *J Am Ceram Soc* 2023, **106**: 6292–6300.
[39] Zhang ZY, Park Y, Xue ZL, *et al.* Research status of bond coats in environmental barrier coatings. *Int J Appl Ceram Tec* 2022, **19**: 1841–1859.
[40] Xue ZL, Mei J, Li F, *et al.* Phase evolution and high-temperature stability of $HfSiO_4$ bond coat for ultra-high temperature environmental barrier coatings. *J Eur Ceram Soc* 2025, **45**: 117102.
[41] Qiu JT, Yang HY, Huang JT, *et al.* High-temperature oxidation resistance behavior and mechanism of $HfSiO_4$-modified C/SiC composites. *Ceram Int* 2024, **50**: 21755–21766.
[42] Leitner J, Voňka P, Sedmidubský D, *et al.* Application of Neumann–Kopp rule for the estimation of heat capacity of mixed oxides. *Thermochim Acta* 2010, **497**: 7–13.
[43] Chen L, Feng J. Influence of HfO_2 alloying effect on microstructure and thermal conductivity of $HoTaO_4$ ceramics. *J Adv Ceram* 2019, **8**: 537–544.
[44] Lyu Y, Du BH, Chen GQ, *et al.* Microstructural regulation, oxidation resistance, and mechanical properties of C_f/SiC/SiHfBOC composites prepared by chemical vapor infiltration with precursor infiltration pyrolysis. *J Adv Ceram* 2022, **11**: 120–135.
[45] Laidler KJ. The development of the Arrhenius equation. *J Chem Educ* 1984, **61**: 494.
[46] Chen Z, Sun XH, Shang YP, *et al.* Dense ceramics with complex shape fabricated by 3D printing: A review. *J Adv Ceram* 2021, **10**: 195–218.
[47] Aramaki S, Roy R. Revised phase diagram for the system Al_2O_3–SiO_2. *J Am Ceram Soc* 1962, **45**: 229–242.
[48] Smialek JL. Oxidation of Al_2O_3 scale-forming MAX phases in turbine environments. *Metall Mater Trans A* 2018, **49**: 782–792.
[49] Ma QS, Cai LH. Fabrication and oxidation resistance of mullite/yttrium silicate multilayer coatings on C/SiC composites. *J Adv Ceram* 2017, **6**: 360–367.
[50] Li H, Yu YP, Fang B, *et al.* High temperature behavior of $HfSiO_4$ subjected to calcium–magnesium–alumina–silicate (CMAS) and high-velocity water vapor. *J Eur Ceram Soc* 2023, **43**: 621–628.
[51] Liu RX, Liang WP, Miao Q, *et al.* Revealing the oxidation growth mechanism and crack evolution law of Si–HfO_2/$Yb_2Si_2O_7$/Yb_2SiO_5/high-entropy hafnate thermal/environmental barrier coatings during thermal cycling. *J Eur Ceram Soc* 2025, **45**: 116979.
[52] Schmücker M, Mechnich P, Zaefferer S, *et al.* Water vapor corrosion of mullite: Single crystals versus polycrystalline ceramics. *J Eur Ceram Soc* 2008, **28**: 425–429.
[53] Liu G, Zhang XF, Lu XY, *et al.* 4D additive–subtractive manufacturing of shape memory ceramics. *Adv Mater* 2023, **35**: 2302108.